NATIONAL ENERGY TECHNOLOGY LABORATORY

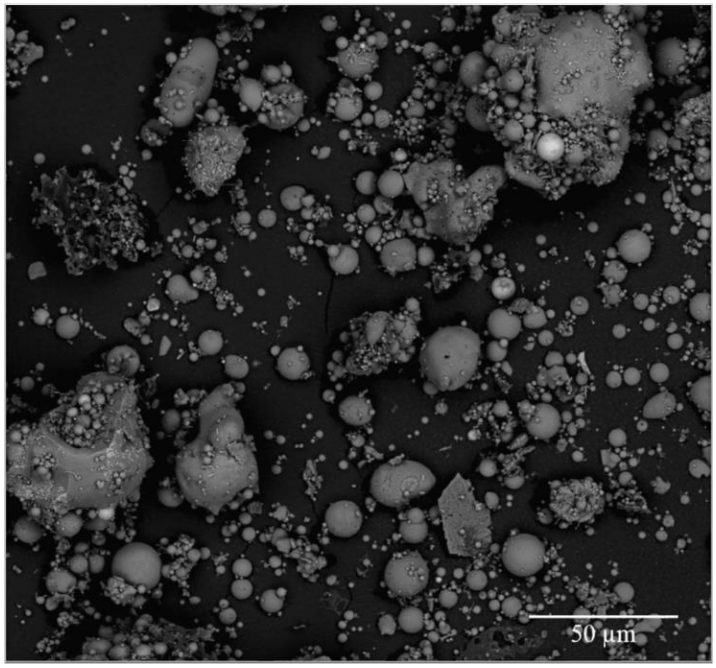

Characterization of Rare Earth Element Minerals in Coal Utilization Byproducts

17 July 2017

Preliminary – Do not cite or quote

U.S. DEPARTMENT OF ENERGY | NATIONAL ENERGY TECHNOLOGY LABORATORY

Office of Fossil Energy

NETL-TRS-10-2017

Disclaimer

Cover Illustration: SEM-BSE image of fly ash particles from sample 251 mounted on a SEM stub.

Suggested Citation: Montross, S. N.; Verba, C. A.; Collins, K. *Characterization of Rare Earth Minerals in Coal Utilization Byproducts*; NETL-TRS-10-2017; NETL Technical Report Series; U.S. Department of Energy, National Energy Technology Laboratory: Morgantown, WV, 2017; p 45.

An electronic version of this report can be found at:

http://netl.doe.gov/research/on-site-research/publications/featured-technical-reports

https://edx.netl.doe.gov/ree

Characterization of Rare Earth Element Minerals in Coal Utilization Byproducts

Scott N. Montross[1], Circe A. Verba[2], Keith Collins[2]

[1] ORISE, Research and Innovation Center, National Energy Technology Laboratory, 1450 Queen Avenue SW, Albany, OR 97321

[2] U.S. Department of Energy, Research Innovation Center, National Energy Technology Laboratory, 1450 Queen Avenue SW, Albany, OR 97321

NETL-TRS-10-2017

17 July 2017

NETL Contacts:

Circe Verba, Principal Investigator

John Baltrus, Technical Team Lead

David Alman, Executive Director, Acting, Research & Innovation Center

This page intentionally left blank.

Table of Contents

List of Figures

List of Figures (cont.)

List of Tables

Acronyms, Abbreviations, and Symbols

Term	Description
CUB	Coal utilization byproducts
REE	Rare earth element
SEM	Scanning electron microscope
EDS	Energy dispersive x-ray spectroscopy
WDS	Wavelength dispersive spectroscopy
EPMA	Electron probe microanalysis
FIB-SEM	Focused ion beam scanning electron microscope
ICP-MS	Inductively coupled plasma mass spectrometry
ICP-OES	Inductively coupled plasma optical emission spectrometry
$(Mg,Al,Mg_5Al,\ Fe)_6(Al,Si)_4O_{10}\ (OH)_8$	Chlorite (Chl)
SiO_2	Quartz (Qz)
Fe_2O_3	Hematite (Hem)
$Ce,La,Nd\ PO_4$	Monazite (Mnz)
$Y,Yb\ PO_4$	Xenotime (Xen)
$(Al_{4.5}Si_{1.5})O_{9.75}$	Mullite (Mul)
$Al_2Si_2O_5(OH)_4$	Kaolinite (Kao)
$KAl_2AlSi_3O_{10}(OH)_2$	Muscovite (Mus)
$ZrSiO_4$	Zircon (Zr)
$FeTiO_3$	Ilmenite (Ilm)
PbS	Galena (Gn)
$BaSO_4$	Barite (Brt)
FeS_2	Pyrite (Py)

Acknowledgments

This work is part of National Energy Technology Laboratory (NETL) research for the Department of Energy's Rare Earth Elements (REE) Program. The authors acknowledge Mary Anne Alvin (NETL Federal Technology Manager), Regis Conrad (REE Program Manager Lead, DOE Office of Fossil Energy), and Charles Miller (Federal Project Manager, Strategic Center for Coal).

The authors also acknowledge Evan Granite and Elliot Roth (NETL-Pittsburgh) for samples. Christina Lopano (NETL-Pittsburgh) for assistance with XRD analysis and technical review of the report. Peter Hseih (NETL-Albany) for technical review of the report. We also thank the Oregon State University Electron Microscopy Facility- Han Chan and Theresa Sawyer- for FIB-SEM data collection and 3D reconstructions. Lastly, we thank Michael Outrequin and Anne-Sophie Robbes from Ametek Inc./Cameca for electron microprobe analysis.

EXECUTIVE SUMMARY

The United States currently produces over 100 million tons of coal utilization byproducts (CUB) per year in the form of fly ash, bottom ash, slag, and flue gas (American Coal Ash Association (ACCA), 2015). But this "waste material" also contains potentially useful levels of rare earth elements (REE). Rare earth elements are crucial for many existing and emerging technologies, but the U.S. lacks a domestic, sustainable REE source. Our project explored the possibility of developing a supply of REEs for U.S. technologies by extracting REEs from CUBs. This work offers the potential to reduce our dependence on other countries for supply of these critical elements (NETL, REE 2016 Project Portfolio).

Geologic and diagenetic history, industrial preparation methods, and the specific combustion process all play major roles in the composition of CUB. During combustion, inorganic mineral phases of coal particles are fluidized at temperatures higher than 1400^{o}C, so inorganic mineral materials are oxidized, fused, disintegrated, or agglomerated into larger spherical and amorphous (non-crystalline) particles. The original mineralogy of the coal-containing rock and heating/cooling of the material significantly affects the composition and morphology of the particles in the combustion byproduct (Kutchko and Kim, 2006). Thus, different types of coal/refuse/ash must be characterized to better understand mineral evolution during the combustion process. Our research focused on developing a working model to address how REE minerals behave during the combustion process: this research should help determine the most effective engineering methods for extracting REEs from CUBs.

We used multimodal imaging and image processing techniques to characterize six rock and ash samples from different coal power plants with respect to morphology, grain size, presence of mineral phases, and elemental composition. The results of these characterization activities provided thresholds for realizing the occurrence of REE mineral phases in CUB and allowed us to calculate structural and volumetric estimates of REE.

Collectively, the rock and coal ash samples contained minerals such as quartz, kaolinite, muscovite/illite, iron oxide (as hematite or magnetite), mullite, and clinochlore. Trace minerals included pyrite, zircon, siderite, rutile, diopside, foresterite, gypsum, and barite. We identified REE phosphate minerals monazite (Ce,La,Nd,Th)(PO_4,SiO_4), xenotime (YPO_4,SiO_4), and apatite ($Ca_5(PO_4)_3$(F,Cl,OH) via SEM and electron microprobe analysis: these materials generally occurred as 1-10 µm-long crystals in the rock and ash samples.

As has been shown in other studies, amorphous material – aluminosilicate glass or iron oxyhydroxide – are the major components of coal fly and bottom ash. Trace amounts of amorphous calcium oxide and mixed element (e.g., Al-Si-Ca-Fe) slag are also present. Quartz, mullite, hematite, and magnetite are the crystalline phases present. We found that REEs are present as monomineralic grains dispersed within the ash, as well as fused to or encapsulated by amorphous aluminosilicate glass particles. Monazite and xenotime have relatively high melting points (>1800 °C) compared to typical combustion temperatures; our observations indicate that the REE-phosphates, which presumably contribute a large percentage of REE to the bulk ash REE pool, as measured by mass spectroscopy, are largely unaltered by the combustion. Our study shows that conventional coal combustion processes sequester REE minerals into aluminosilicate glass phases, which presents a new engineering challenge for extracting REE from coal ash.

The characterization work summarized in this report provides a semi-quantitative assessments of REE in coal-containing rock and CUB. The data we obtained from 2- and 3-D imaging, elemental mapping, volumetric estimates, and advanced high-resolution pixel classification successfully identified the different mineral phases present in CUB. Further, our characterization results can guide techniques for extracting REEs from CUB, or other geologic and engineered materials. Whilst, interpretations will inform future REE separation and extraction techniques and technologies practical for commercial utilization of combustion byproducts generated by power plants.

1. INTRODUCTION

Since 1985, the United States has consumed more than 800 million tons of coal per year with nearly 90% used for electricity generation (US-EIA Energy Review, 2016). Coal burning electric utilities produce over 100 million tons of CUB annually (ACA, 2014). The U.S. Department of Energy (DOE) defines CUB as fly ash, boiler slag, fluidized-bed combustion ash, or flue gas desulphurization materials produced from the combustion of coal or the cleaning of stack gases (US-DOE Topical Report 24). Industrial and engineering uses for CUB, specifically fly ash, has reduced fly ash waste. However, nearly 75 million tons of CUB are disposed of in landfills or storage ponds annually (ACA, 2014).

The combination of geologic and diagenetic history, industrial preparation methods, and the specific combustion process determines the physical and chemical composition of CUB produced by power plants (Taggert et al., 2016; Brownfield et al., 2005). Domestic coal resources and combustion byproducts from energy generation are a viable source of REE (Ketris and Yudovich, 2009; NETL-EDX). Given the reliance on imported REE, there is a need to increase domestic production for several sectors of the U.S. economy (e.g. catalysts, electronics, magnets, batteries, and other applications related to national security and energy independence).

REE concentrations are reported for coal beds and coal fly ash (Rozelle et al., 2016; Franus et al., 2015; Hower et al., 2013; Shatzel et al., 2003; Hower et al., 1999; Zwarwick et al., 1997) and typically exceed estimates of REE concentrations in the upper continental crust (Rudnick and Gao, 2012). Estimates of REE concentration for Ce and La in the upper continental crust are reported by Rudnick and Gao (2012) and references within. The average concentration of Cerium (Ce) and lanthanum (La) in the upper continental crust are approximately 63 and 31 mg/kg respectively (Rudnick and Gao, 2012). Hard coal (e.g., bituminous and anthracite) and hard coal fly ash tend to have the highest REE content of all geologic material (Rudnick and Gao, 2012; Ketris and Yudovich, 2009). Global averages for Ce in soft coal (brown lignite) and hard (including bituminous to anthracite) are 22 and 23 ppm respectively. Brown and hard coal fly ash contain nearly 6x the amount of Ce (Ketris and Yudovich, 2009). Ce and La concentrations in CUB may be as high as 397 and 560 mg/kg respectively in certain combusted fly ashes (NETL-EDX). Higher than average concentrations of rare earths in CUB along with the abundance of CUB available for mining make coal and associated combustion byproducts a viable target for REE resource recovery.

REE trends in CUB are predominantly based on the origin of feed coal. A study of major coal feedstocks in the United States, ranked coal from different geographic locations based on REE content (Taggert et al., 2016). Average total REE content in Appalachian coal combusted ashes studied was ~591 mg/kg and greater than Illinois and Powder River Basin coals, 403 and 337 mg/kg respectively. The authors demonstrated that the concentration of major elements (Al, Si, and Fe) made the ash particles vary between coal sources. Most notably is the difference in the percentages of SiO_2, Al_2O_3, and Fe_2O_3 in the ash, specifically the major elemental signatures for three coal regions; Appalachian (high Si and Al, low Ca), Illinois Basin (high Fe, low Ca), and Powder River Basin (low Si and Al, high Ca).

Studies on the mobility of elements during coal combustion have shown that REE may be homogeneously distributed as nano-sized particles in amorphous aluminosilicate glass (Hower et al., 2013; Mardon and Hower, 2004). Mardon and Hower (2004) and Hower (1999) also demonstrated the impact source coal properties and combustion techniques such as temperature,

blend, and ash collection points have on the quality and composition of the combustion byproducts and associated REE. A related study demonstrated the occurrence of REE in carbonatite and other Ca-bearing minerals in igneous systems, where vaporization, condensation and crystallization of minerals from the melt is analogous to the formation of solid inorganic mineral particles (e.g., ash particles) during coal combustion and collection in the bag house (Hower et al., 2013). Of interest are Ca-bearing mineral phases in source rock and coal reject (e.g., Ca-silicate, calcite and apatite) and CUB (calcium oxide) due to a known dependence on Ca content and substitution of REE into certain mineral phases (Mulrooney and Rivers, 2005).

A combination of X-ray diffraction (XRD), acid extraction and bulk elemental analysis are typically used to determine the bulk geochemical composition of materials and can be used to provide reasonable quantification of REE for resource estimates or valuation of assets (Soco et al., 2007). While these methods are suitable for basic assessment, they do not provide the detailed mineralogical information that is crucial to the development of targeted extraction methods. For this study, we combined the results of bulk geochemical analysis, microscopy/imaging, and X-ray microanalysis to characterize different coal and CUB samples (3 fly ash, 1 bottom ash, 1 roof rock, and 1 pulverized coal reject) to provide a more robust account of the presence and occurrence of REE in coal and CUB. The objective of this work is to characterize CUB samples that are representative of byproducts produced during the utilization of coal in power generation systems. Pulverized reject, produced ash, and disposed materials from coal utilization all provide REE recovery opportunity and this work aimed to provide detailed elemental and mineral phase data for CUB to aid in the discovery of targeted, higher efficiency extraction techniques that bring REE resources into the market in the safest, most efficient, and most economically viable way.

This report describes the collaborative effort between researchers from NETL, Oregon State University Electron Microscopy Facility, and Amtek Inc./Cameca to develop a workflow that can be used for characterization of REE in different materials; provide quantitative assessments; and guide extraction of REE resources from geologic and/or other engineered materials. Using multimodal microanalytical imaging and image processing techniques, we describe the morphological, elemental, and mineralogical properties of each sample with a focus on the inorganic mineral types present (e.g., oxides, phosphates, sulfates, sulfides) and the occurrence of REE.

Our characterization provides an endpoint assessment of the mineralogical and elemental composition of coal ash and provides context to the partitioning of particular elements of interest (REE) into minerals that are formed during combustion. Our results provide quantitative structural, chemical, and morphological estimates of particle type and mineral phases, including REE-minerals, in source material and combustion byproducts. Our data and interpretation of the mineral phases present in the different sample types that were analyzed provides a more representative assessment of available REE resource in CUB, allowing better resource evaluation of materials such as fly ash waste or other byproducts of mining and energy production suitable for the recovery of critical resources.

2. MATERIALS AND METHODS

2.1 SAMPLE PREPARATION

Four ash and two rock samples with REE concentrations greater than 300 ppm were chosen for advanced characterization (Fig. 1). The samples were selected from the NETL Research and Innovation Center database housed on the Energy Data Exchange website.

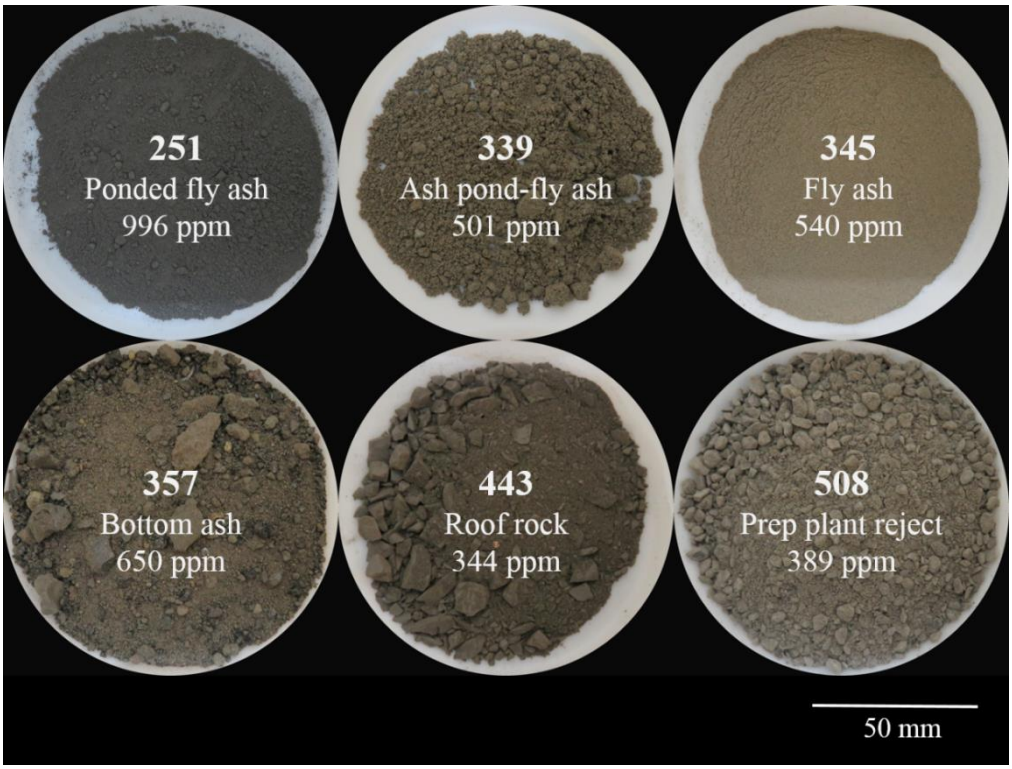

Figure 1: Photographs of samples analyzed and sample type. Total REE concentrations (Lanthanides + Y) are based on bulk analysis using ICP-MS.

Prior to analysis, the samples were dried in an oven at 55^{o}C for 8 hours and stored in a nitrogen-purged desiccator for 72 hours. The bulk sample was mixed thoroughly and subsamples were taken for XRD (5 g) and SEM microanalysis (2 g). Samples for XRD were ground to < 63µm and prepared as random mounts. For microscopy and microanalysis, each sample was mounted as a powder grain mount on double stick carbon tape affixed to a metal SEM stub and a 1 or 3-inch diameter epoxy mount. The epoxy-mounted samples were ground sequentially with 80, 100, 220, 500, 600, 800, and 1200 grit metal/diamond grinding wheels, pre-polished with diamond suspensions (6 and 1-µm).A final polish was applied using 0.05 micron aluminum polishing solution.

2.2 X-RAY DIFFRACTION

Bulk mineralogy of rock and ash samples was determined by X-ray diffraction (XRD) of a randomly oriented powder mount. Powdered samples were mounted on an automatic 6-position

sample changer with spinner. XRD patterns were collected using a Rigaku III Ultima diffractometer equipped with Cu anode. The samples were scanned at 40kV, 44mA utilizing Cu radiation over a range of 3.0 – 65 two-theta with a step size of 0.02 and a scan time of 2.4 seconds. Phase IDs, peak alignments and mineral identifications were made via comparison of the diffraction peaks against the ICDD-4 database. Qualitative analysis of the crystalline components of the samples was performed using the whole peak-fitting module in Jade 6.0. Quantitative XRD analysis was performed on fly and bottom ash samples. Ash samples were initially ground via a ball mill using a ZrO2 grinding jar. The ground materials were then spiked with 10% Al_2O_3 and lightly ground under acetone in a mortar and pestle to homogenize. The ground material was mounted in a stainless steel cavity spinner mount and set up on the autochanger. The scans were all run over 4-70 deg 2-theta (Cu) on a PANalytical X'Pert Pro instrument equipped with copper radiation and the X'Celerator detector. Basic Rietveld fitting was performed using the PANalytical HighScore Plus software to quantify mineral percentages and estimate amorphous content (wt %).

2.3 MICROSCOPY AND MICROANALYSIS

Polished and grain-mounted samples were evaporatively coated with ~10 nm of Pd. A field emission-scanning electron microscope (FE-SEM, FEI Quanta V) equipped with an energy-dispersive X-ray spectrometer (EDS, Oxford Instruments) was used to observe the microstructure of the material and collect elemental data with accompanying backscatter electron (BSE) images. SEM imaging and EDS analysis was done at 20 kV, ~100nA; WD=10mm, beam aperture 3, and spot size 5.0-5.5nm. Standards-based quantitative EDS was achieved using certified rare earth element standards for phosphates (REEP25-15+FC, Astimex Standards Ltd.) and oxides (Standard block #489, Geller Microanalytical Laboratory). Electron Probe Microanalysis (EPMA) was conducted on a CAMECA SX Five electron probe outfitted with BSE, EDS, and WDS detectors. EPMA imaging was done at 15keV, 95nA, and 25ms dwell time. Elemental X-ray maps for REE and P were acquired by WDS and maps for Al, Si, and Ca acquired by EDS. Standardized quantitative EDS microanalysis was performed by comparing spectra collected from certified standards with spectra from the sample. Both were collected on the same instrument and under the same operating conditions. Rare earth phosphates standard REEP25-15+ FC (Astimex Standards Ltd.) and oxides standard #489 (Gellar Analytical) were used for all analyses. Standard block #489 is certified to ISO 9001 and 17025 standards. Mineral phase identification was done manually using the collective results from ICP-MS, XRD, SEM imaging, and X-ray microanalysis by SEM/EPMA-EDS or EPMA-WDS.

Scanning electron microscopy was employed to "point count" ash particles in the samples. Approximately 0.2 g of each sample was sprinkled onto double-sided carbon tape mounted on a 1-cm diameter SEM stub. Backscattered images (1000x magnification) were collected from five randomly chosen fields of view per sample. This magnification was chosen to not exclude smaller (~1-micron) particles. Measurements of sphere diameter and length of agglomerated particles (b-axis length) were made manually using the measurement tool in the FIJI software tool. Accompanying EDS point measurements and full field elemental maps were collected to aid in the identification/composition of particle types. Particle dimensions are reported in microns and averages for each sample were calculated from fields of view that contained 30-300 individual particles per field of view. The fraction of amorphous glass that was less than 1 micron in size was not included as a sphere or agglomerated particle in the particle distribution

measurements due to the inability to resolve and correctly measure individual particles at the magnification chosen for the point counts.

The volumetric extent of REE phases was investigated using focused ion beam scanning electron microscopy (FIB-SEM) on characterized samples. Two sites were chosen in the rejected pulverized coal sample (508) based on fields of interest identified during previously conducted electron microscopy and elemental analysis. These sites were prepared for milling at high current in a Helios dual beam FIB-SEM. A Pt pad (20-50 nm) was put down on the sample at the milling location to protect the sample during milling and prevent curtaining during image acquisition. Once the hogout trench was completed using Fe_2O_3 as the source material, fiducials were set and milling was conducted at a 52^o angle. Analytical conditions for REE 508 site of interest 1 were; 2 kV, e-beam current = 400 pA, number of slices = 466, slice thickness = 15 nm/slice, x = 34.44 micron, y = 31.11 micron, z = 6.99 micron and at site of interest 2: e-beam voltage = 2 kV, e-beam current = 800 pA, number of slices = 179, slice thickness = 15 nm/slice, x = 28.54 micron, y = 27.7 micron, z= 2.69 micron.

2.4 ADVANCED IMAGE PROCESSING

Backscattered electron images and elemental maps of individual grains were collected on independent single fields of view (up to 1024 fields of view at ≥4,000x magnification per run) and larger areas were imaged and montaged together using Oxford INCA software. This technique allowed identification and mapping of the distribution of REE minerals and other mineral phases in CUB samples over a 1-cm^2 area of the sample. Elemental data is displayed as an overlay on BSE images or as CAMEO images. CAMEO images are color-enhanced images where each color represents a distinct range of X-ray emission spectra to create distinct phases. Pixel classification and object/phase identification was performed on individual, stacks of multiple images, and montaged SEM images using Ilastik 1.1.9 software. The distribution and occurrence of features, and particle morphology in the classified images was quantified using FijiIsJustImageJ (FIJI) software.

REE mineral phases were identified by SEM-BSE; elements were quantified by EDS; and FIB-SEM images (where applicable) were combined to determine REE by mass. Individual tomographic image slices acquired from FIB-SEM were realigned and reconstructed and features of interest were segmented using FEI Avizo9 Digital Rock Physics software. Once the distribution volumes of REE-phosphates were constructed, the weight percent of Ce, La, and Nd, (measured by EDS) was used to calculate the mass of REE in the mineral phase. The occurrence of REE minerals in the sample were tracked and quantified using digital image files generated by pixel and object classification and analysis techniques.

Characterization data and advanced image processing using montaged BSE and elemental maps were used to provide both qualitative and quantitative analyses for REE minerals and other mineral phases of interest in CUB. Our methods were designed and successful at (1) determining the bulk mineralogy of each sample using XRD and performing semi-quantitative analysis of peak patterns to determine the relative abundance of minerals in the sample; (2) discovering REE mineral phases in rock and ash samples, including individual crystals of monazite (Ce, La, Nd-PO_4) and xenotime (Y-PO_4) and; (3) imaging the morphology and determining the chemical composition of REE bearing minerals, amorphous glass, and other particles and rock fragments in the samples.

3. RESULTS

3.1 CHARACTERIZATION OF ROOF ROCK AND COAL REJECT

Reject coal and flint clay are predominantly composed of shale and clay grains. Diffraction patterns for samples 508 (coal reject) and 443 (flint clay) are shown in appendix figure A-1. A summary of XRD results are shown in Table 1 along with a qualitative estimate of the amount of each mineral identified in the samples. Reject coal and flint clay have similar mineralogical compositions and contain quartz, kaolinite, muscovite/illite, plagioclase, and calcite. No REE minerals were identified by XRD analysis. Bulk chemical composition of the samples was calculated using ICP-MS data. The chemical composition (in weight % oxide) of the material in samples 508 and 443 is Si (66-71%), Al (21%), Fe (5%), and Ca (0.1-0.5%).

Table 1: XRD analysis results with qualitative estimates of abundance for each crystalline phase

	SAMPLE ID	
PHASE	443	508
Quartz	Major	Major
Kaolinite	Minor	Intermediate
Muscovite/Illite	Trace	Minor
Calcite	Trace	Trace
Plagioclase	Trace	Trace

*major (>50%), intermediate (25-50%), minor (5-25%), and trace (<5%)

XRD patterns confirmed the presence of various clays in roof and reject rock samples. However, the material was not oriented prior to XRD analysis so the clay minerals are grouped into a general category of phyllosilicates. SEM analysis provides morphological and elemental data to better identify clay minerals present—specifically kaolinite (Si, Al-rich member) and Clinochlore/Chlorite— and crystallographic interstratified clay minerals are also possible.

In addition, the roof rock (sample 443) and prep plant reject rock (sample 508) contain trace REE- phosphate minerals (e.g. —monazite and xenotime) and zircon that are embedded between bedding layers of muscovite and/or kaolinite (Fig. 2). Iron in the reject and roof rock is primarily associated with pyrite, chlorite, or siderite but may also be present as amorphous or poor crystalline oxides/hydroxides. Individual minerals identified by SEM-EDS analysis are quartz, muscovite, clinochlore, monazite, xenotime, pyrite, siderite, barite, titanium oxide, ilmenite, sphalerite, and zircon.

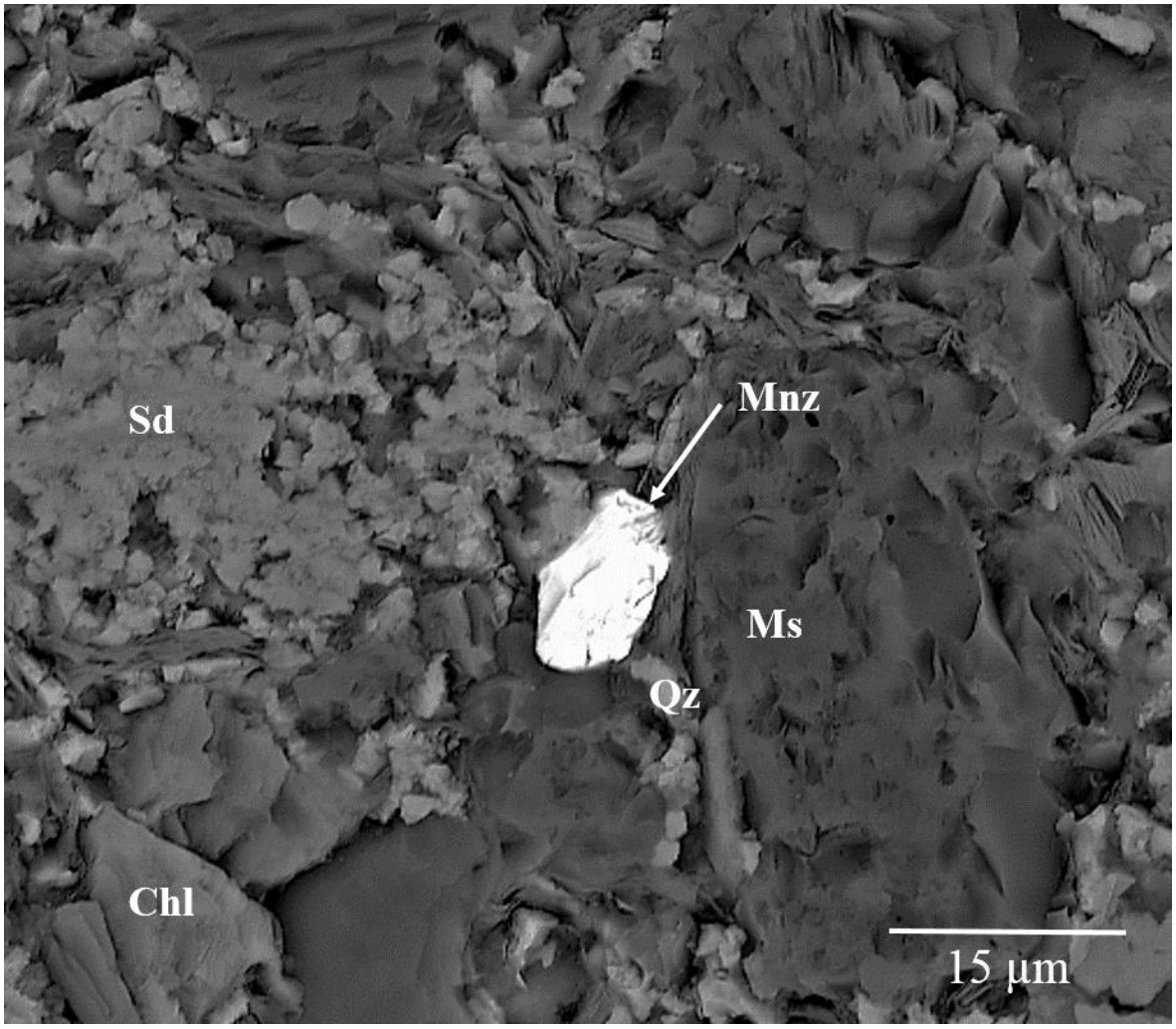

Figure 2: SEM-BSE image of monazite (Mnz) in matrix muscovite from prep plant reject rock sample 508. Mineral abbreviations are Qz=quartz, Ms=muscovite, Sd=siderite, Chl =chlorite.

3.1.1 Sample 443: Flint Clay Roof Rock

Sample 443 is a flint clay roof rock that consisted of dark gray to black rock fragments (Fig. 1) that were waxy and exhibited conchoidal parting, likely due to the presence of kaolinite. The chief mineral constituents determined by XRD are quartz and mixed phyllosilicates from kaolinite and/or muscovite/illite groups (Table 1).

Trace mineral phases identified by SEM in the sample were monazite, xenotime, hematite, barite, pyrite, ilmenite, and titanium oxide. Hematite and ilmenite made up the majority of the metal bearing trace minerals in the rock matrix (Fig. 3).

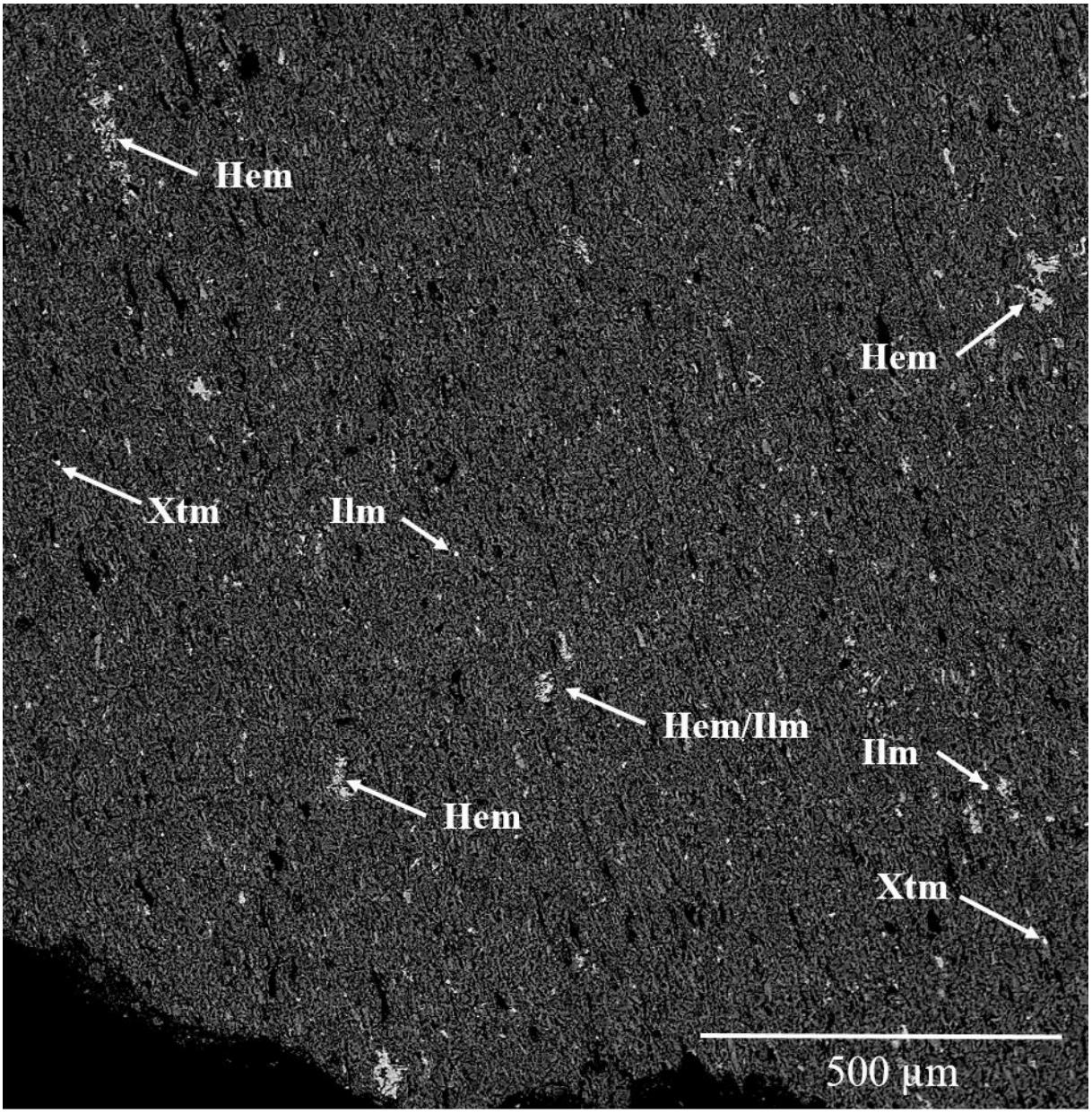

Figure 3: SEM-BSE image of flint clay roof rock matrix (Sample 443) and accessory minerals. Mineral abbreviations are Hem=hematite, Py=pyrite, Ilm=ilmenite, Hem=hematite, Xtm=xenotime.

Pyrite existed as isolated framboids in pore space of the rock. Ilmenite was present in the sample (<1%) as a whole and co-existed with nickel cobalt sulfide that contained approximately 1% La, Hf, and Zr. The REE phosphates – monazite and xenotime, which are enriched in La, Ce, and Nd – were typically 1-5 µm long florets among the platy matrix grains of muscovite and kaolinite. Examples of accessory minerals identified by SEM-EDS –xenotime, clinochlore, kaolinite, pyrite, ilmenite, and hematite– are shown in Fig. 4.

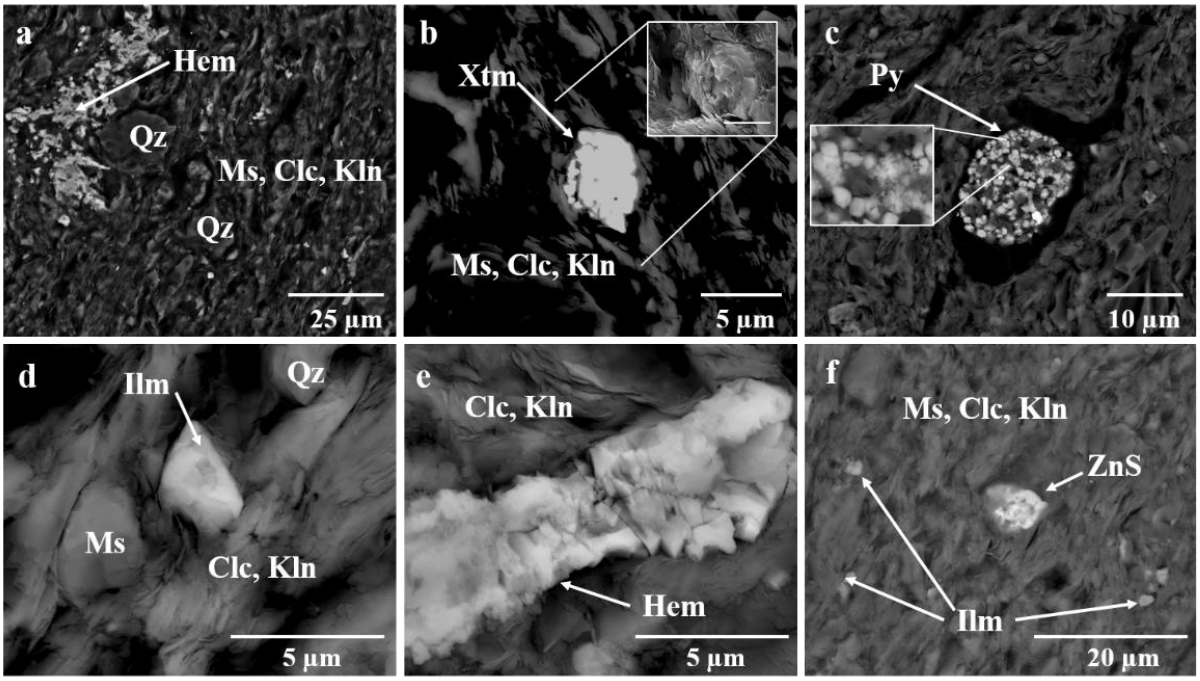

Figure 4: SEM-BSE images of accessory minerals in sample 443. Hematite (a,e), xenotime (b) and secondary electron image of the mineral (inset of b), pyrite (c), ilmenite (d,f) and zinc sulfide (f) in the flint clay roof rock matrix. Mineral abbreviations used are Qz=quartz, Hem=hematite, Ms=muscovite, Clc=clinochlore, Kln=kaolinite, Py=pyrite, Ilm=ilmenite, Hem=hematite, Xtm=xenotime.

3.1.2 Sample 508: Heavy Media Cyclone Reject

The Heavy Media Cyclone Reject sample was composed of a fine powder fraction and larger, rounded rock fragments (1-10 mm diameter) that were brown to light grey. The larger fragments were relatively homogenous in size (Fig. 1). The individual grains were layered with extensive pore space (Fig. 5). The chief mineral constituents determined by XRD were quartz, muscovite, and kaolinite (Table 2). SEM analysis of rock grains showed abundant framboidal pyrite clusters in pore spaces and between layers in the clay matrix (Fig. 5 and 7c).Chlorite grains were composed of the endmembers clinochlore (Mg, Al) and chamosite (Fe, Al) (see Fig. 6a).

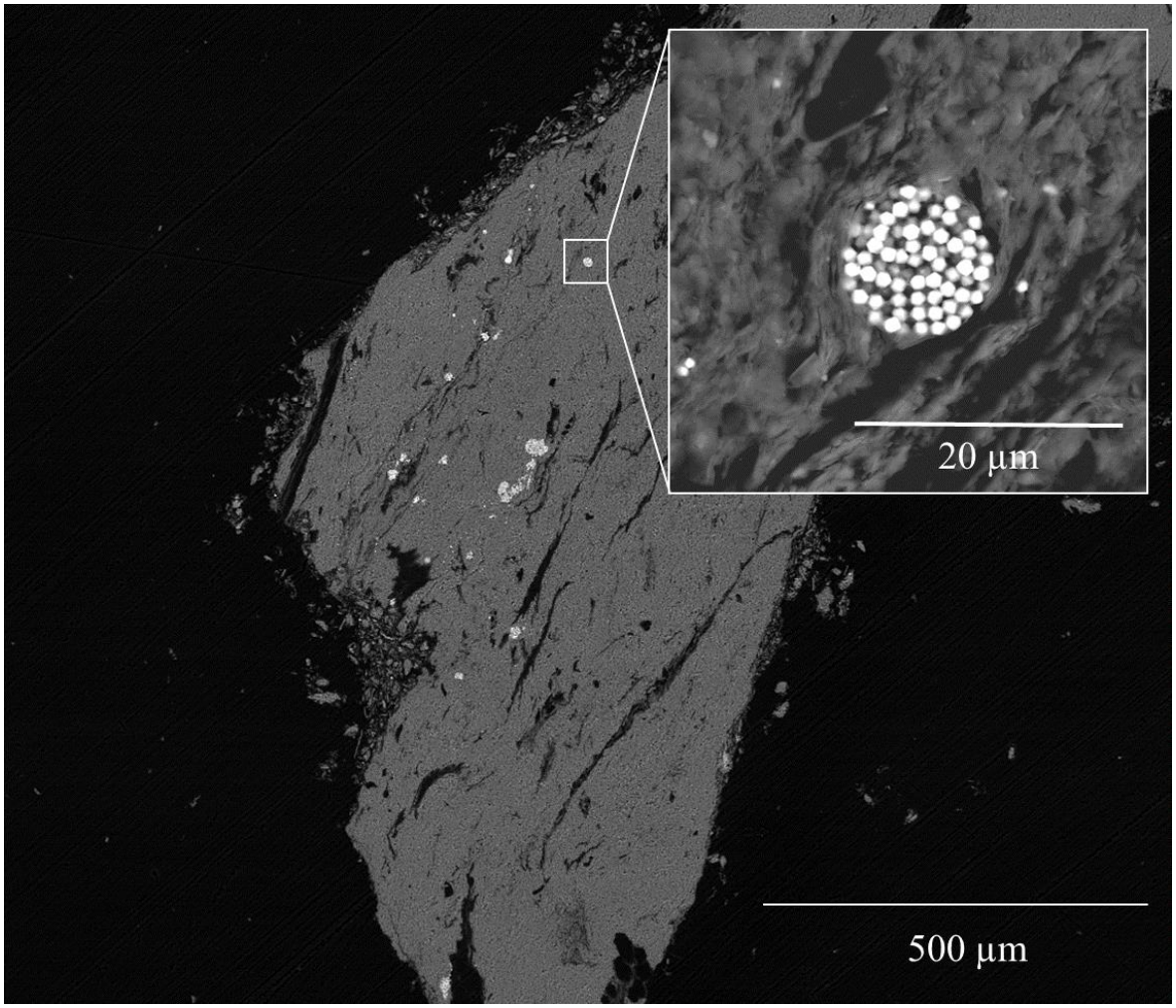

Figure 5: SEM-BSE image of a rock fragment from sample 508. The reject rock fragment is composed of quartz, muscovite, and kaolinite with framboidal pyrite in the clay matrix (inset) and pore space.

Monazite and xenotime mineral grains were present in each of the rock grains examined. The REE minerals ranged in size from 1-10 μm long and were located in pore space within the rock matrix (Fig. 2, 6, and 8). They were typically found adjacent to clinochlore, muscovite, and kaolinite mineral grains (Fig. 2 and 6). Monazite was also present as individual mineral crystals in the fines portion of the sample. These grains were likely dislodged from rock grains during prep plant pulverization. Pore spaces filled with pyrite did not contain monazite or xenotime.

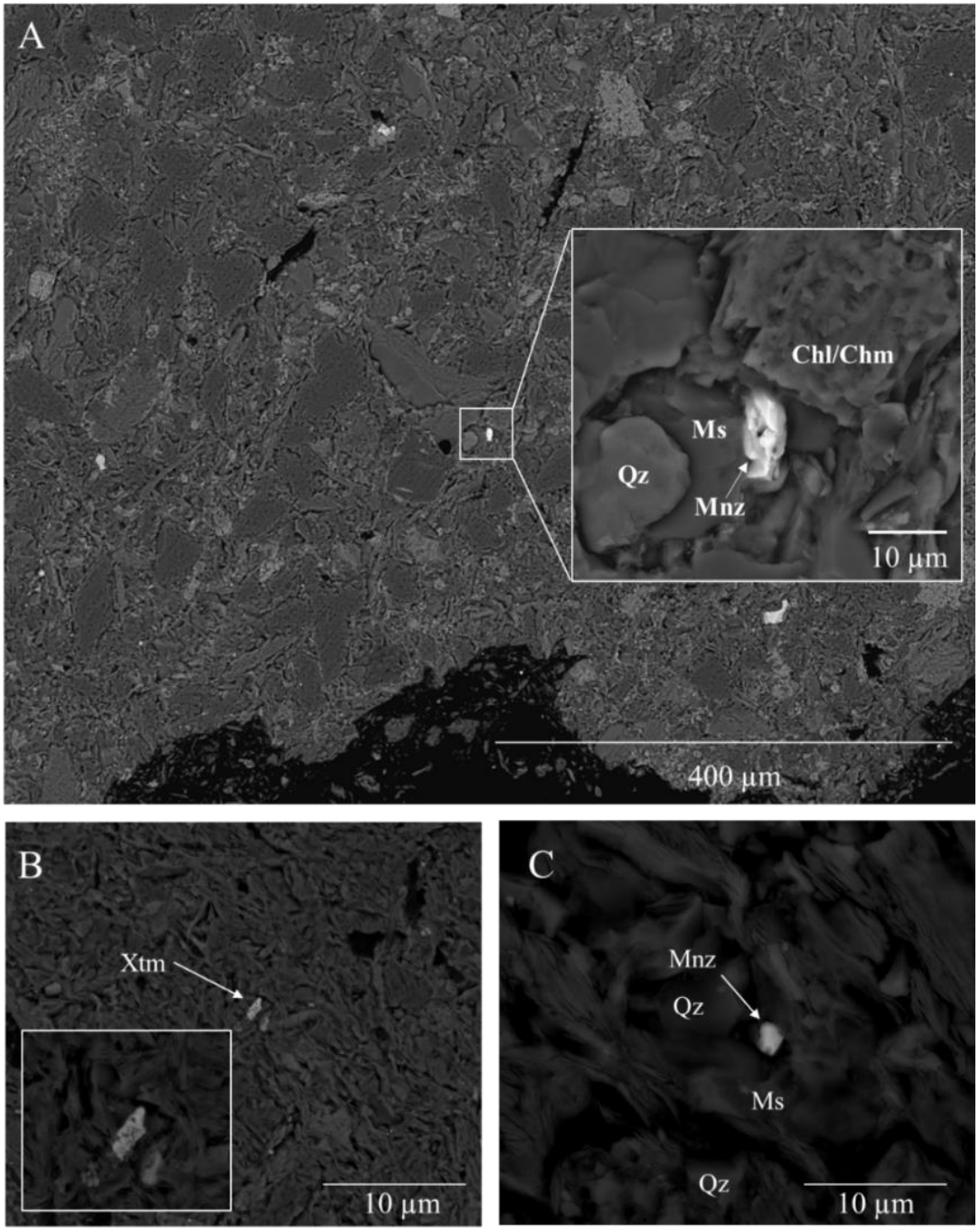

Figure 6: SEM-BSE image of REE-phosphate minerals monazite (A, C) and xenotime (B) in matrix muscovite from reject coal sample 508. Mineral abbreviations are Qz=quartz, Ms=muscovite, Chl=chlorite, Chm=chamosite, Xtm=xenotime, Mnz=monazite.

Trace minerals present in the sample were zircon, barite, sphalerite, and galena (Fig. 7). No REE was detected in zircon (Fig. 7a), galena (Fig. 7b), or barite (Fig. 7e-f) or in the clay grains adjacent to these minerals. Pyrite in the sample contained approximately 1% La and Hf (Fig. 7c).

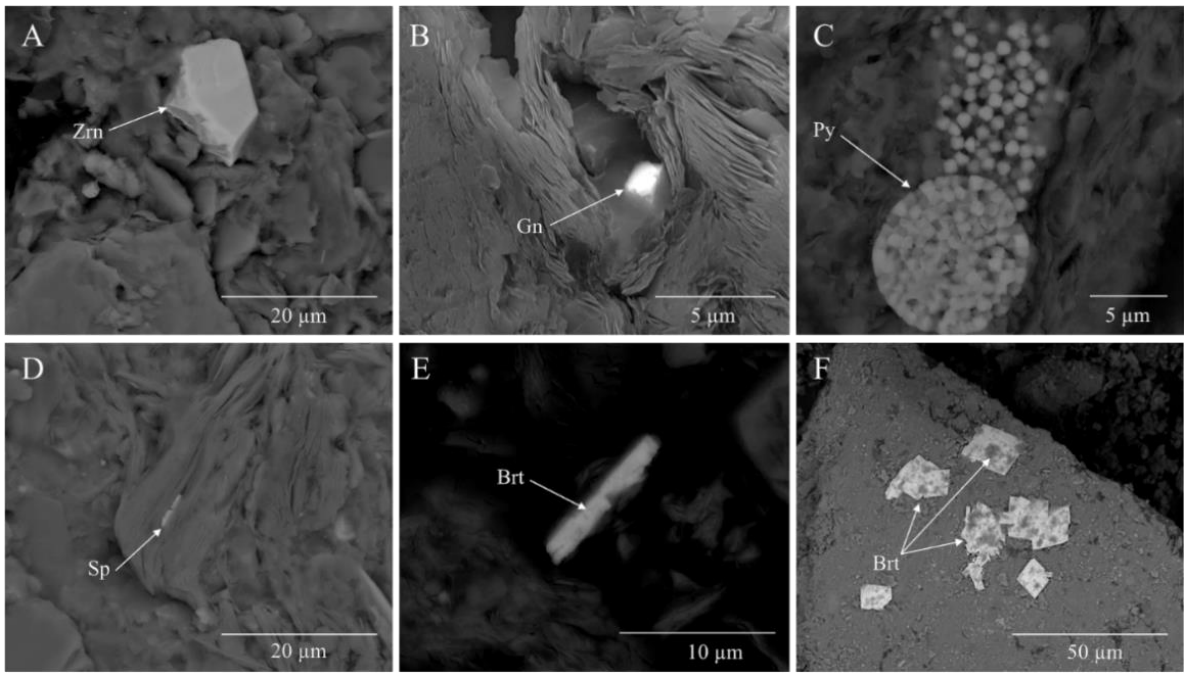

Figure 7: SEM-BSE images of examples of non-REE trace minerals present in coal reject rock 508. Mineral abbreviations are Brt=barite, Sp=sphalerite, Zrn=zircon, Gn=galena, Zrn=zircon.

Three-dimensional reconstructions and image analysis allowed for quantitative estimations of the volume of specific minerals of interest. The coupled results of SEM-EDS and FIB-SEM analyses provided a qualitative analysis of the internal geometry of rare earth mineral grains (e.g., monazite) and the matrix rock. FIB-SEM was conducted on an area of interest that contained a monazite grain embedded in muscovite/phyllosilicate (Fig. 8a,b) that contained the elemental composition of (in weight %) Ce (27.6%), La (11.2%), Nd (9.9%), and Pr (2.3%) as measured by SEM-EDS.

Reconstructed images demonstrated the geometry of the monazite grain in the rock matrix (Fig. 8c) and allowed for calculation of the volume of the REE grain or other mineral phases of interest. The total volume of the monazite grain shown in figure 8 is 187.1 μm^3 with an estimated 0.266 ng Ce, 0.108 ng La, and 0.095 ng Nd. This technique can be used to upscale based on the distribution measured by pixel counts to compare to the bulk composition.

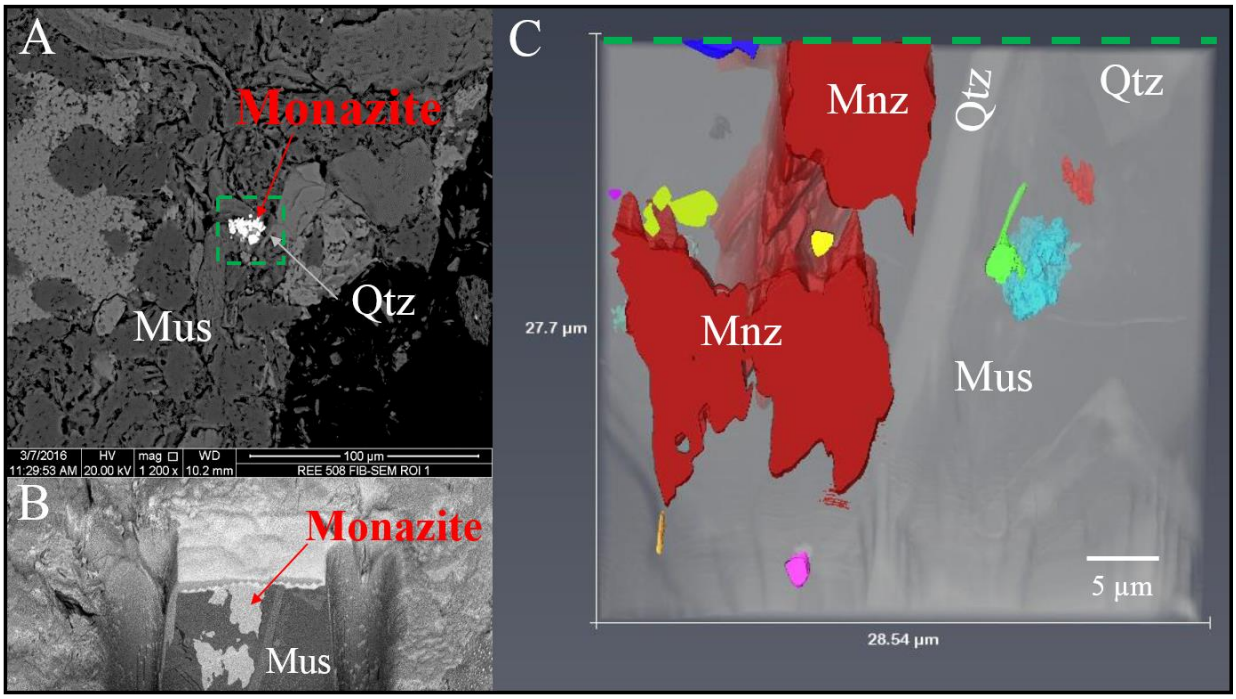

Figure 8: Analysis of coal refuse (508) by field emission SEM coupled with a focused ion beam (FIB-SEM). (A) SEM-BSE image of site of interest for FIB-SEM analysis containing monazite (Mnz), muscovite (Mus), and quartz (Qtz). The green box denotes the area analyzed by FIB-SEM. (B) Z-contrast image of the milled site of interest. (C) Three dimensional reconstruction of FIB-SEM images showing accessory mineral phases in the sample.

3.2 CHARACTERIZATION OF FLY AND BOTTOM ASH

XRD analysis of the ash materials showed that the predominant crystalline components are quartz, mullite, hematite, and magnetite (Fig. A-1; Table 2). A summary of quantitative XRD results are shown in Table 2. Hematite (enriched with Ti), magnetite, and mullite are exclusive to ash samples in this study and were not detected in roof rock or reject rock samples by XRD (Fig. A-1; Tables 1 and 2). Fly ash and bottom ash samples contained amorphous glass particles, mixed element slag, solid non-spherical particles, cenospheres (hollow and spherical Al/Si particles), and solid spherical particles (see Fig. 9). Organic particles were present, and consisted of unburnt carbon particles and char plerospheres (carbon cage). Particles had surface coatings/crusts common for multiple particles joined together by mineral flocculation.

Non-crystalline (amorphous) particles, likely a mix of aluminum and silicon oxide and iron oxyhydroxide, comprised a majority of the material in ash samples (Table 2). Amorphous glass particles are composed primarily of aluminum, silicon, and oxygen and referred to as aluminosilicate glass. Mixed element slag was found in all samples and generally contained some proportion of the elements Al, Si, Ca, K, and Fe. Cenospheres and solid Al/Si particles (See Fig. 9) were present in all samples.

Table 2: Quantitative XRD analysis results for fly and bottom ash samples. Values are in weight %.

	SAMPLE ID			
PHASE	**251**	**339**	**345**	**357**
Quartz	11	8	6	2
Mullite	16	9	7	6
Hematite (Ti)	<1	3	3	4
Magnetite	<1	3	8	3
Rutile	<1	--	--	--
Diopside	--	--	--	2
Forsterite	--	<1	<1	--
Gypsum	--	--	--	<1
Amorphous	62	66	66	71

Solid Al/Si-rich spheres/pellets are composed of slag and typically contain trace to minor concentrations of Fe, K, and Ca. Iron oxide was present in all samples as solid spheres, non-spherical particles, and as coating and crust on ash particles (Fig. 11). In some cases, the iron oxide was titanium (Ti) rich; specifically, ilmenite hematite with Ti replacement identified in all ash samples.

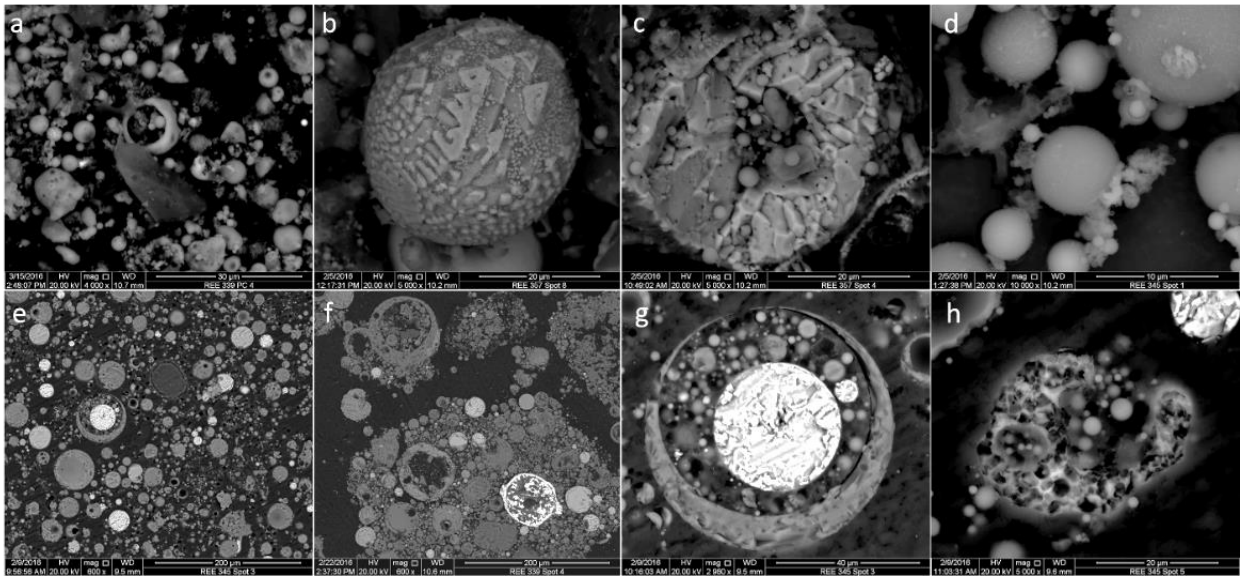

Figure 9: SEM-BSE images of examples of different types of ash particles present in the suite of samples. The samples shown were prepared as grain (a-d) and epoxy (e-h) mounts. Fly ash samples are composed of Al/Si cenospheres (a,c-h), Fe/Ti oxide spheres and pellets (b-c and e-h), solid Al/Si spheres/pellets (e-g), Al-Si slag and agglomerated particles (e-h), REE mineral grains (a and e-f) and Ca-Si-Al oxides (h).

Point count results revealed the relative distribution (major>moderate>minor>trace) of particle types in the samples (Appendix Table A-1). Fly ash samples 251 and 339 contained minor amounts of mixed Fe-oxide and aluminosilicate spheres. Iron-titanium rich spheres were most abundant in fly ash sample 339 (medium) and in bottom ash sample 357 (minor). All samples contained Ca-oxide (trace to minor) particles. However, in 345 and 357, Ca-oxides make up between 15-20% (minor) of the total particles. Bottom ash sample 357 and fly ash sample 345 contained minor concentrations of agglomerated particles. The most abundant and largest sized agglomerated particles were observed in bottom ash sample 357. Monazite was observed as isolated crystals in the ash matrix in multiple fields of view in sample 345. No REE minerals were observed in point count fields of view for samples 251, 339, and 357.

Particle sizes for spheres and agglomerated particles varied between fly and bottom ash samples (See Appendix Fig. A-2 and A-3). In general, fly ash particles had the smallest average sphere diameter. The average diameter for fly ash spheres were 4.3, 4.1, and 2.4 µm for samples 251, 345, and 339 respectively. The average sphere diameter for bottom ash sample 357 was 8.4 µm. In all ash samples >93% of the glass spheres had a diameter <10 µm (Table 3). The largest diameter sphere encountered was 102 microns in the bottom ash. Inversely the smallest diameter spheres were measured in fly ash samples 251and 339 at approximately 0.4 µm. Agglomerated particles, masses of smaller particles joined together by glass, slag, or mineral flocculation were most abundant and had the largest diameter in the bottom ash sample (357).

The metal oxide content of ash samples, calculated using element concentrations determined by ICP-OES/MS, are shown in Table 3. All samples were class F ashes with a $SiO_2+Al_2O_3+Fe_2O_3$ >70%; silicon dioxide is the most abundant metal oxide in the samples. Calcium oxide (CaO) in ash samples ranged from 0.9 and 4.0 (wt %).

Table 3: Size distribution of spheres and metal oxide content of fly and bottom ash samples

Sample ID Sample Type	251 Fly ash	339 Fly ash	345 Fly ash	357 Bottom ash
Size distribution of spheres (%)				
0.07-10.0 µm	93.6	98.7	98.6	76.5
>10.0 µm	6.4	1.3	1.4	23.5
Metal oxide content (wt%)				
SiO_2	71.8	60.9	62.0	61.5
Al_2O_3	26.9	19.5	19.8	17.9
Fe_2O_3	4.4	15.6	18.0	23.5
CaO	0.9	2.5	4.0	2.4
Whole sample total REE (ppm)	**996**	**501**	**540**	**650**

Fly ash sample 345 had the highest CaO content of the ash samples analyzed and Ca was distributed throughout the sample in a variety of different particles (Fig. 10) such as porous irregularly shaped grains or solid mineral slag pellets (Fig. 11). Calcium oxide rich grains were porous, filled with smaller cenospheres and solid particles, and may have had a fibrous micro texture (see Fig. 11).

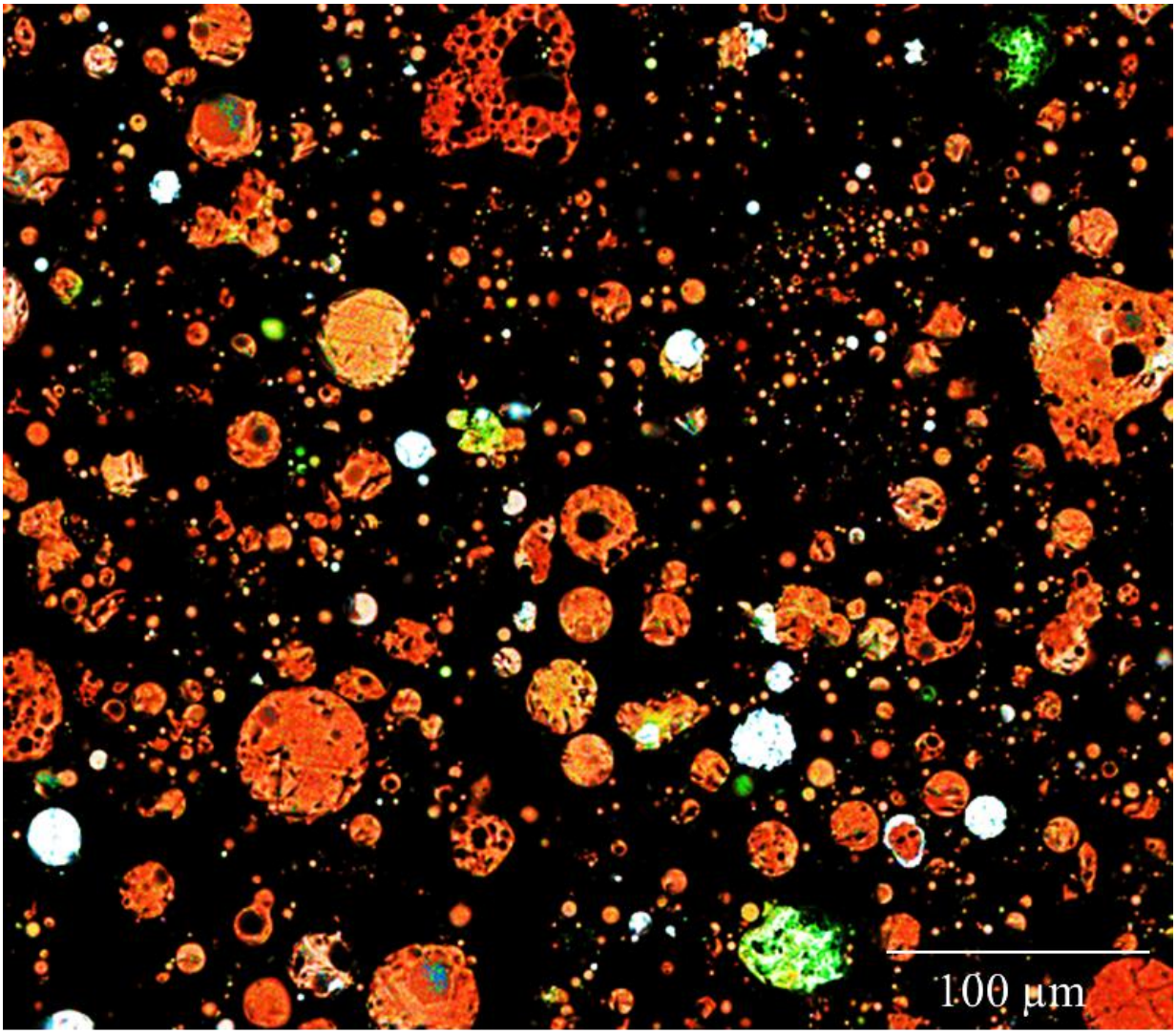

Figure 10: SEM-BSE image of epoxy mounted fly ash from sample 345. Overlain is a CAMEO elemental map showing distribution of major elements in the sample. Color scheme Al/Si-rich (red-orange), Ca-rich (green), and Fe-rich (blue to white).

REE concentrations, determined by bulk ICP-MS analysis are shown in Table 3 (data from Pittsburgh Analytical Laboratory-PAL). Both monazite and xenotime were observed as individual crystals in the ash matrix and encapsulated by aluminosilicate glass or mixed element slag. REE was also detected in Ca-rich slag. The presence and occurrence of REE minerals in each sample are presented in sections 3.2.1-3.2.4 of this report.

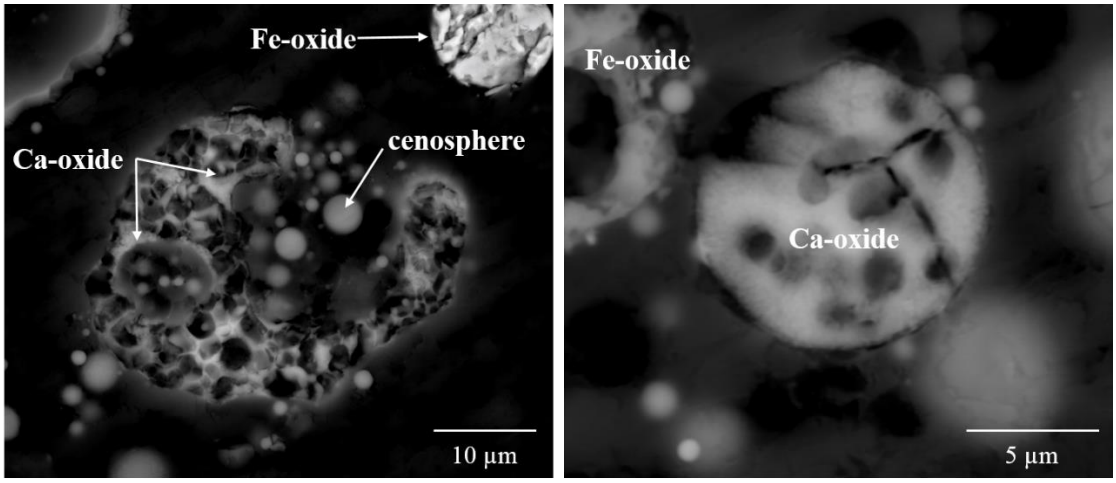

Figure 11: SEM-BSE image of porous calcium oxide, iron oxide, and cenospheres (left) and solid calcium oxide particle (right) from fly ash sample 345.

3.2.1 Sample 251: Ponded Fly Ash

Sample 251 is a fly ash composed primarily of aluminosilicate spheres and, to a lesser extent, Al/Si and Fe/O mixed spheres. The morphology of the particles were spherical, non-spherical (oval or oblong), crystalline, and agglomerated particles (Fig 12; Appendix Table A-1). Particle sizes in this sample (both spherical and non-spherical) ranged from 0.1 to 140 µm and consisted of hollow cenospheres, solid spheres, agglomerated particles, unburnt carbon, char plerospheres, and fragments of inorganic mineral material such as quartz and partially decomposed muscovite (Figs. 12-14; Appendix Table A-1). More than 50% of the spherical particles were aluminosilicate spheres (Appendix, Table 1; Fig. A-2,3). The largest sphere diameter measured was 59 microns (See Fig. A-2). Nearly 94% of the spheres are <10 µm in diameter (Table 3). Microspheres <10 µm in diameter tended to be uniformly spherical. Mixed Ti/Fe-Si/Al rich spheres were approximately 20% of the total spheres. This estimate included aluminosilicate spheres with a Fe/O coating. However, in the larger size fractions (>25 µm) up to 60% of the spheres were Fe/Ti rich and contain little to no Al or Si.

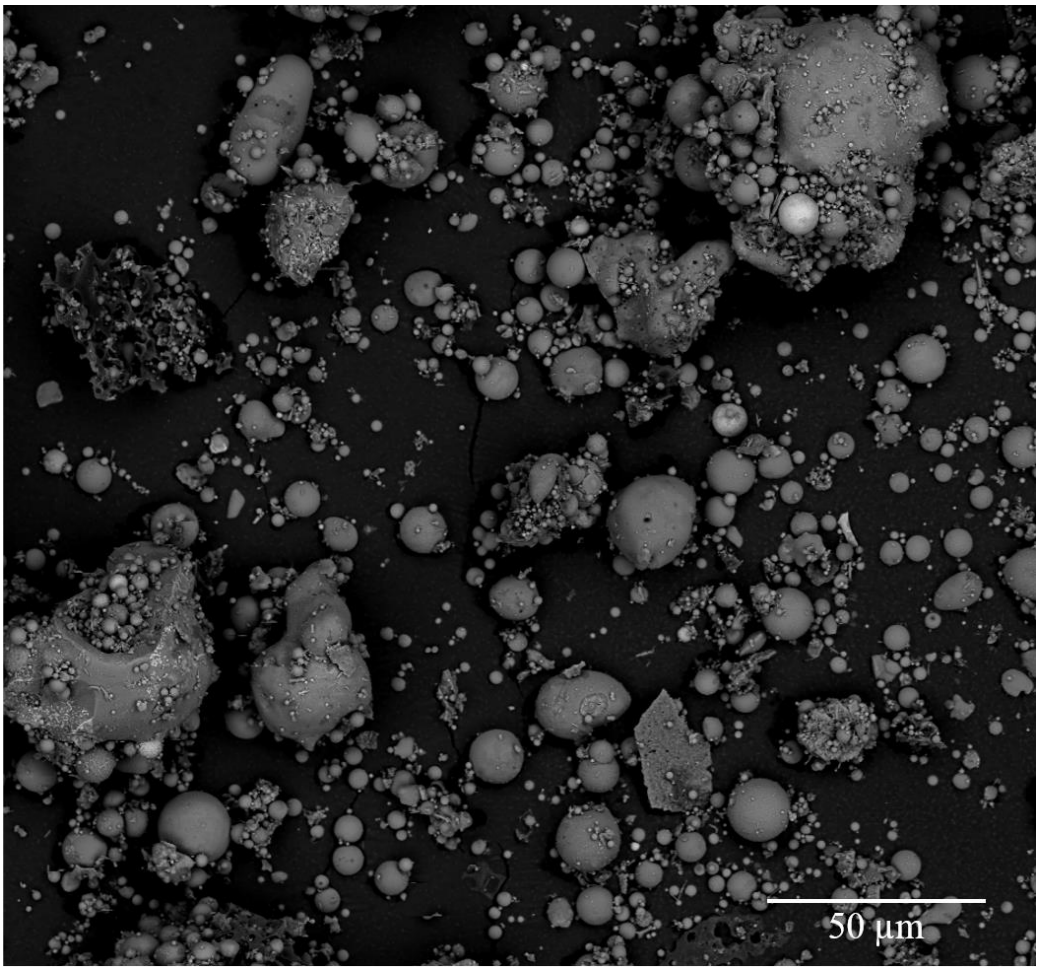

Figure 12: SEM-BSE image of a grain mount with fly ash particles from sample 251.

Mullite, quartz, and hematite were the crystalline phases present in fly ash sample 251 (Table 2). XRD pattern baseline was raised from 13º to 40º (2θ) which indicated the presence of amorphous material (Fig. A-1). Amorphous aluminosilicate particles were present as spheres and irregularly shaped glass particles (Fig. 13 and 14 a,d,f). Silicon (as SiO_2) and aluminum (as Al_2O_3) were the most abundant metals in the sample (Table 3). Smaller spherical particles were bound by slag, aluminosilicate glass, or a carbon "cage", herein referred to as a char plerosphere (Fig. 14c).

Large agglomerated particles were present and composed of smaller particles of aluminosilicate-rich rich material (e.g., cenospheres, solid slag pellets, and glass), iron/titanium oxide, and CaO particles. The concentration of elements K, Ca, S, and P were all below 1 wt. percent in amorphous aluminosilicate glass and spheres. The average composition of mixed element slag in weight percent was Si (37%), Al (22%), O (24%), K (6%), Fe (5%), Ti (4%). Calcium, magnesium, and copper was generally >0.5-1.0 wt%. Char plerospheres were present and classified as agglomerated particles (Fig. 14c). The C plerospheres were generally >50 um diameter and filled with aluminosilicate-rich particles and Fe oxide microspheres (Figs 12 and 14) and other mineral particulates.

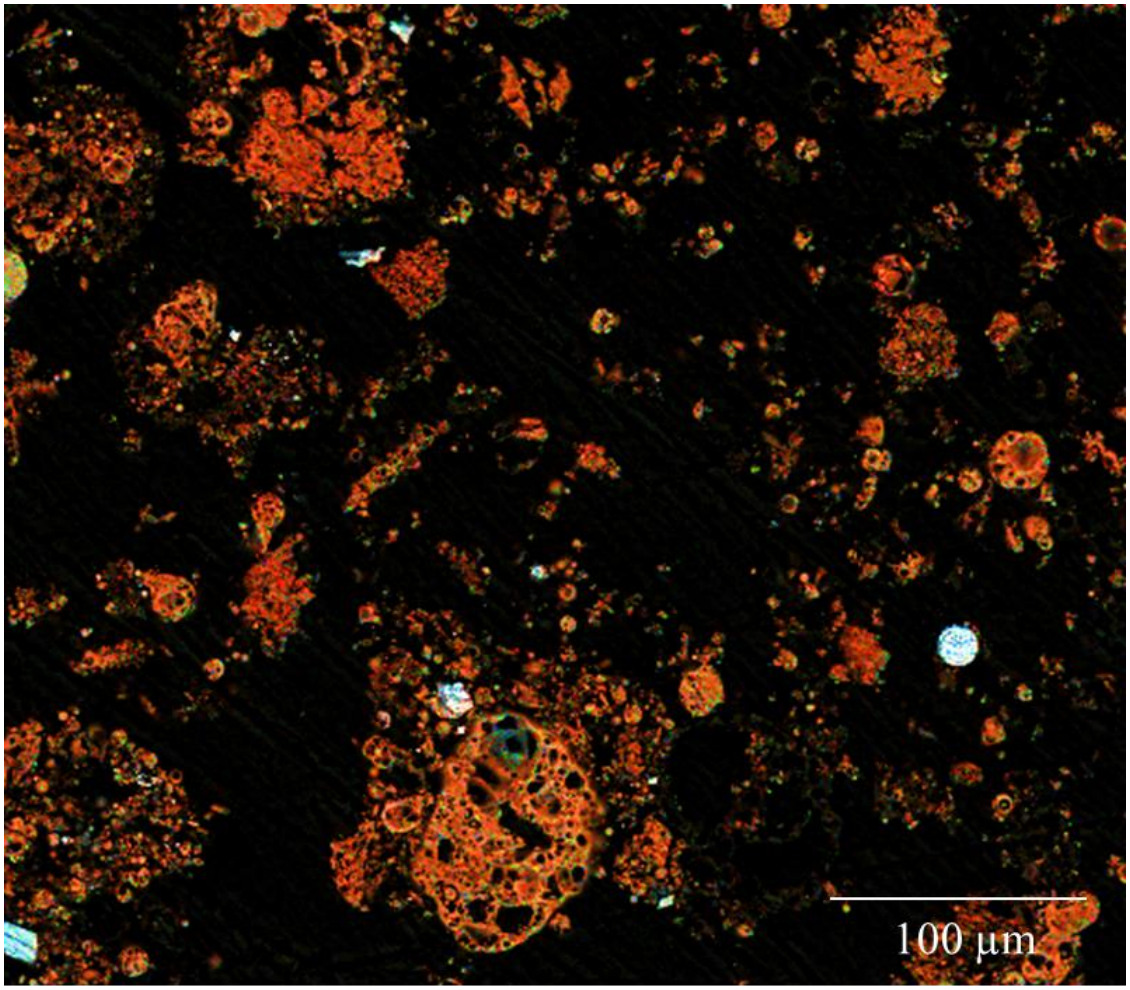

Figure 13: SEM-BSE image and CAMEO elemental map of fly ash grains from sample 251 showing distribution of major elements in the particles. Color scheme Al/Si (red-orange), Ca (green), and Fe (blue to white).

Potassium was evenly distributed in slag particles and the material that coats other particles. Iron oxide (likely hematite) occurred as solid pellets (Fig. 13) and mineral crusts on particles (Fig. 14d).

Monazite and xenotime were not identified in the sample by XRD and no REE-bearing mineral crystals or mixed REE grains were identified by SEM-EDS analysis (>0.1 wt%). REE were not detectable by EDS in iron oxide coatings, carbon fragments, slag or aluminosilicate glass. Mineral crusts and overgrowths on the surfaces of particles (Fig 12 and Fig. 14c,d) were abundant. However, the crusts were thin (sub-micron to single micron thick) and made detection and quantification of elements in the crust difficult due to EDS analysis excitation volume being greater than the feature of interest.

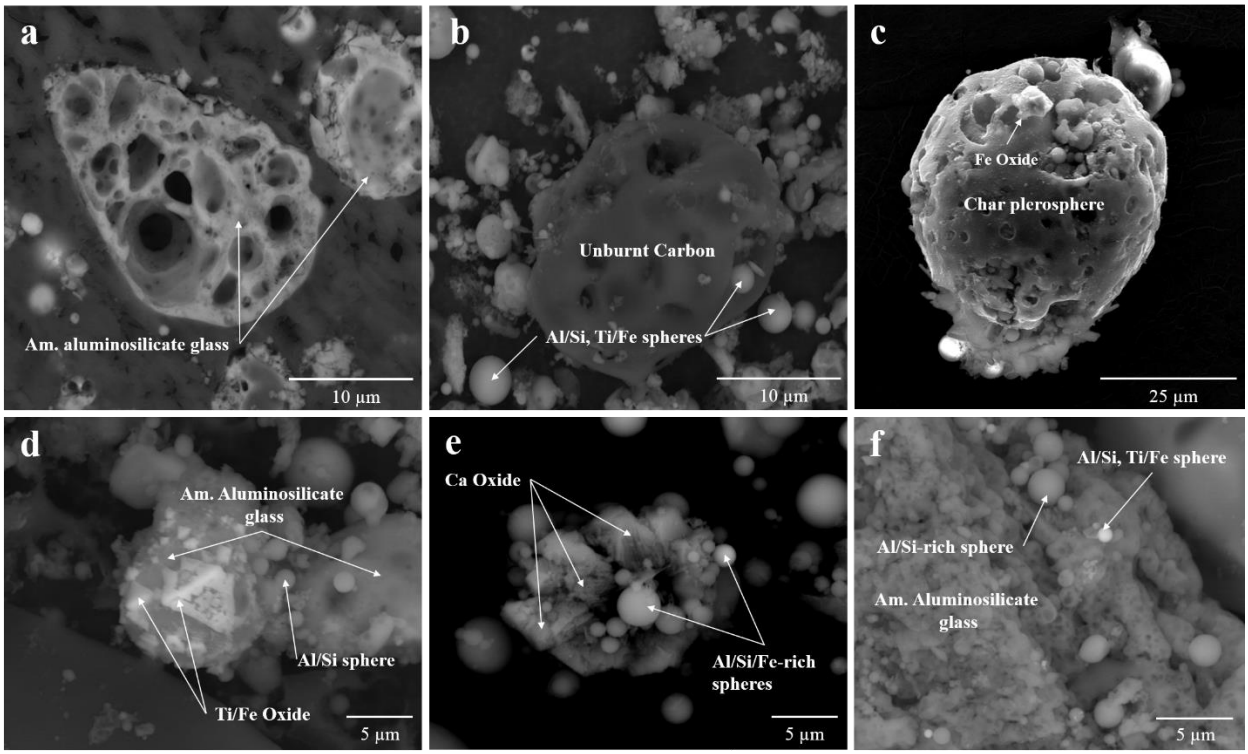

Figure 14: SEM-BSE images of the predominant particle and mineral types in fly ash sample 251. Amorphous aluminosilicate glass and Al/Si-rich spheres (a-f), carbon particles (b,c), iron and titanium oxide (c,d) and calcium oxide (e).

3.2.2 Sample 339: Ponded Fly ash

Sample 339 was a fly ash that contained a variety of different particle types (Fig. 15). Cenospheres and other aluminosilicate particles were the most abundant particle type in the sample analyzed. Hollow Fe spheres and aluminosilicate particles containing Fe were also present in moderate abundance (Fig. 15, 16 and Appendix, Table A-1). Non-spherical particles consisted of Al/Si-rich slag (Fig. 15-17), unburnt carbon (Fig. 17), and barite ($BaSO_4$) crystals (Fig 16). Inorganic crystalline minerals in the sample were composed of Si, Al, Fe, and Ca (Fig. 15-17). Amorphous aluminosilicate glass was present in a range of sizes and a matrix of small glass particles was present and abundant in high magnification images (Fig. 17). Morphology and elemental data indicate that approximately 25-50% of the sample was composed of amorphous aluminosilicate spheres and slag. The remaining proportion was Fe/Ti-oxide spheres, unburnt carbon and crystalline inorganic mineral material. Trace amounts of carbon plerospheres and fragments of carbonaceous material (Fig. 16 and 17) denoted as unburnt carbon (UC) were also observed in the sample. The particle size in this sample (both spherical and non-spherical) ranged from 0.1 to 83 µm (Appendix Fig. A-2 and A-3) with no spheres >13.9 microns. Microspheres that were <10 µm in diameter tended to be uniformly spherical. Large particles (>15 micron) in the sample were oblong shaped cenospheres (Fig. 15 and 17) agglomerated particles, unburnt carbon, and Al/Si slag.

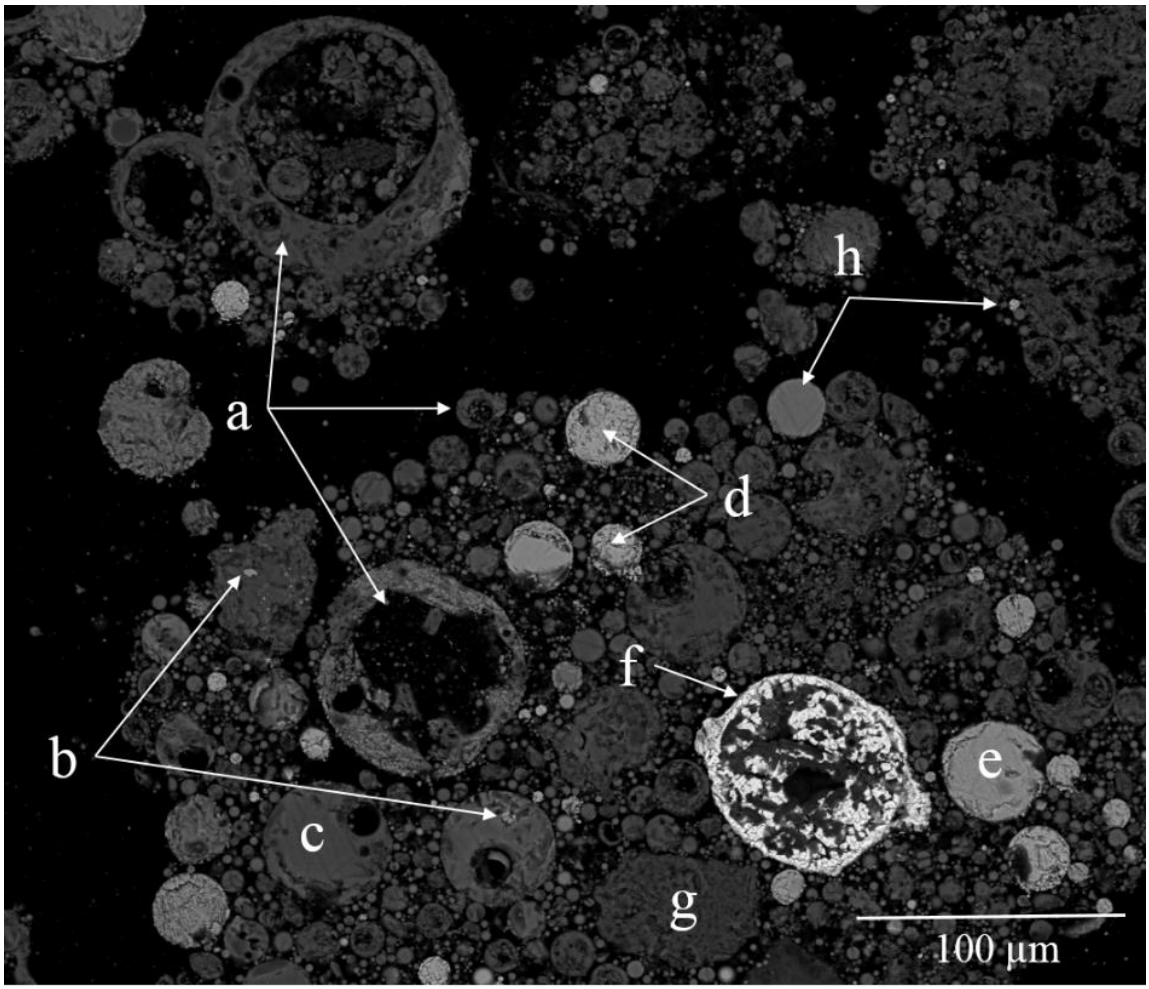

Figure 15: SEM-BSE image of fly ash grains from sample 339 mounted in epoxy. The letters denote different particle types that were identified based on morphology and chemical composition. Cenospheres (hollow aluminosilicate spheres) filled with particles (a), encapsulated mineral grains in slag (b), Solid Al/Si slag droplets (c), solid Fe spheres (d), mixed Fe, aluminosilicate particles (e), Hollow Fe/Ti particle (f), amorphous mixed element slag (g), and Ca oxide (h).

Barite, iron oxide, and copper carbonate made up the bright minerals seen in the SEM-BSE images (Fig. 15). Barite exists as individual crystals within the ash or attached to amorphous slag from combustion (Fig. 16). Because the melting point for barite is ~1580^{o}C, it is plausible that barite did not form during combustion, but rather was sourced from the coal stock feed.

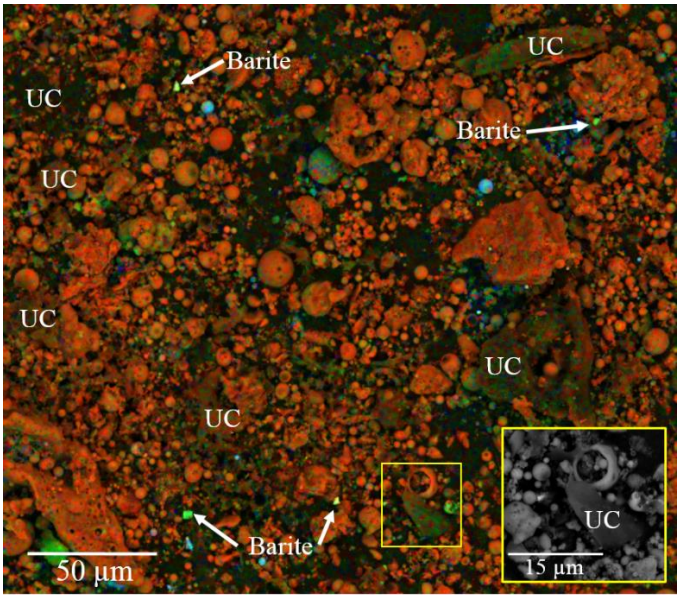

Figure 16: SEM-BSE and CAMEO elemental map of fly ash grains from sample 339 showing distribution of major elements in the sample. Color scheme Al, Si (red-orange), Ca or Ba (green), and Fe (blue to white). Fragments of unburnt carbonaceous material are labeled UC.

Lastly, no monazite or xenotime crystals were identified in sample 339 fly ash. Spot analysis and mapping of multiple particles by EDS failed to detect REE in Al/Si glass, Fe/Ti spheres, unburnt carbonaceous material, or and crusts/coatings.

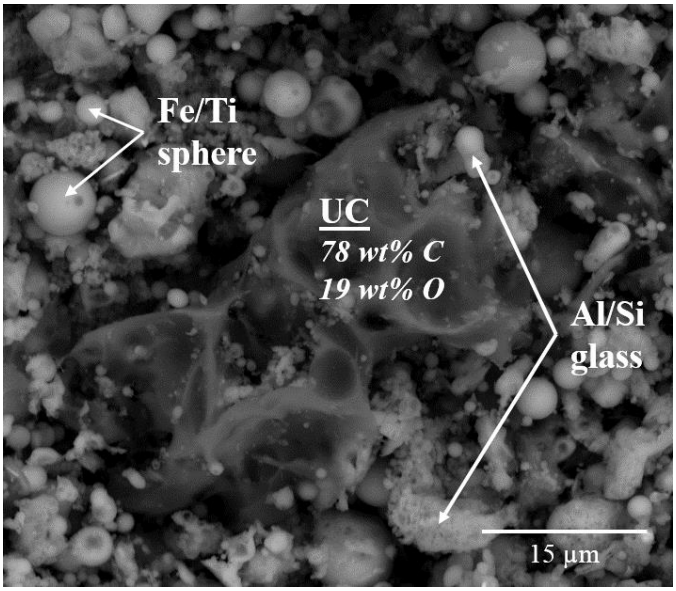

Figure 17: SEM-BSE image of fly ash particles from sample 339. Shown is an unburnt carbon particle among amorphous aluminosilicate glass and mixed iron/titanium spheres.

3.2.3 Sample 345: Fly ash

Sample 345 is a fly ash that was composed of cenospheres, solid iron spheres, Al/Si/Ca slag pellets, aluminosilicate glass, and solid Ca oxide particles (Fig. 18). The major mineral constituents identified by XRD are quartz, hematite and mullite. The suite of minerals identified by coupled XRD and SEM-EDS were: quartz, mullite, ilmenite, hematite, zircon, apatite, calcium oxide and monazite. Amorphous phases present were mixed element slag, aluminosilicate spheres (e.g., cenospheres), and glass.

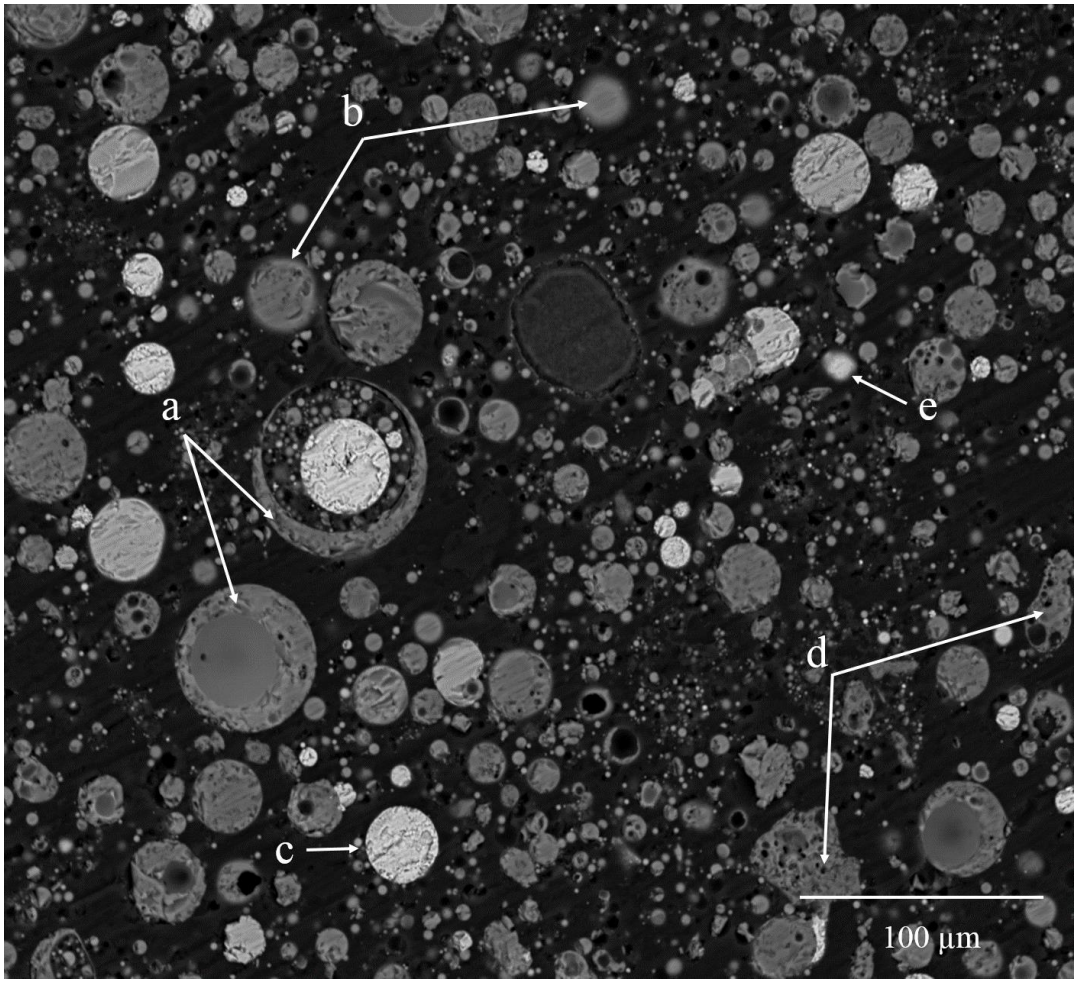

Figure 18: SEM-BSE image of fly ash particles from sample 345 mounted in epoxy. The letters denote examples of the different particle types determined by morphology and chemical composition. Cenospheres empty or filled with particles (a), Solid Al/Si/Ca slag droplets (b), solid Fe spheres (c), aluminosilicate glass (d), Ca oxide (e).

More than 50% of the total particles were aluminosilicate spheres. Nearly 90% of the spheres were less than 4 µm in diameter (Appendix, Table A-1 and Fig. A-2). The sample contained minor amounts (5-25%) of agglomerated particles. Agglomerated particles were up to 40 microns long and 80% of the particles were less than 19 µm in length (Appendix, Fig. A-3). Calcium was present as calcium oxide in porous and fibrous solid particles (Fig. 10, 11 and

Appendix, Table A-1) and Ca-rich slag pellets (Fig. 18). Fragments of decomposed mineral material were also present and make up ~5% of the total particles (Appendix, Table A-1).

Large spherical particles (>10 µm) with higher intensity BSE signal (see Fig. 18) than aluminosilicate particles were composed of iron and/or titanium oxide (likely hematite or ilmenite). Both hematite and ilmenite mineral solids were abundant on the surface of aluminosilicate particles as mineral overgrowths (Fig. 19).

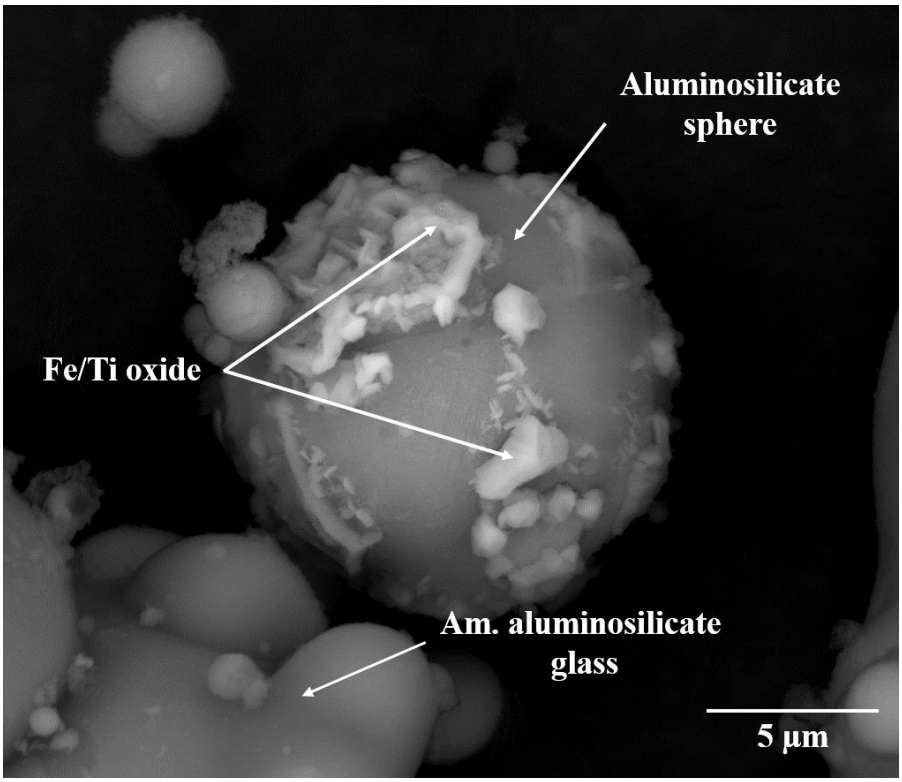

Figure 19: SEM-BSE image from sample 345 of aluminosilicate fly ash particle with iron oxide mineral crust and overgrowths.

Amorphous aluminosilicate glass spheres and mixed element (Al/Si/Ca) slag also contained micron sized dendritic iron oxide needles embedded in the surface of particle (see Fig. 19). Solid spherical Al/Si/Fe slag pellets contained amorphous aluminosilicate glass particles that were encapsulated by the slag. Figure 20 shows an example of a ~60 µm diameter aluminosilicate plerosphere filled with microspheres, slag droplets, solid hematite particles, and a grain of monazite.

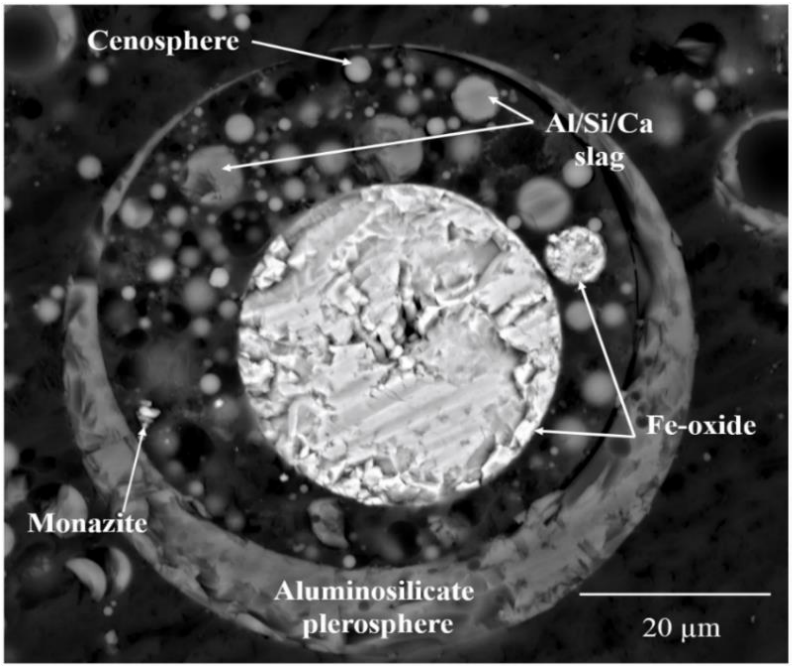

Figure 20: SEM-BSE image of an aluminosilicate plerosphere from sample 345 packed with smaller ash particles and mineral debris.

Most notable, is the ~1 µm long monazite grain that appears to be fused to a fragment of aluminosilicate glass, and lies within the large outer plerosphere. A mosaic of EMPA-BSE images (375 images total) reveled six grains of monazite in the ash matrix (Appendix, Fig. A-4). The rare earth minerals identified in the sample are present as individual crystals in the ash matrix (Fig. 21) and crystals encapsulated in amorphous aluminosilicate particles (Fig. 22; Appendix, Fig. A-5) or fused to aluminosilicate glass (Fig. 20; Appendix Fig. A-5).

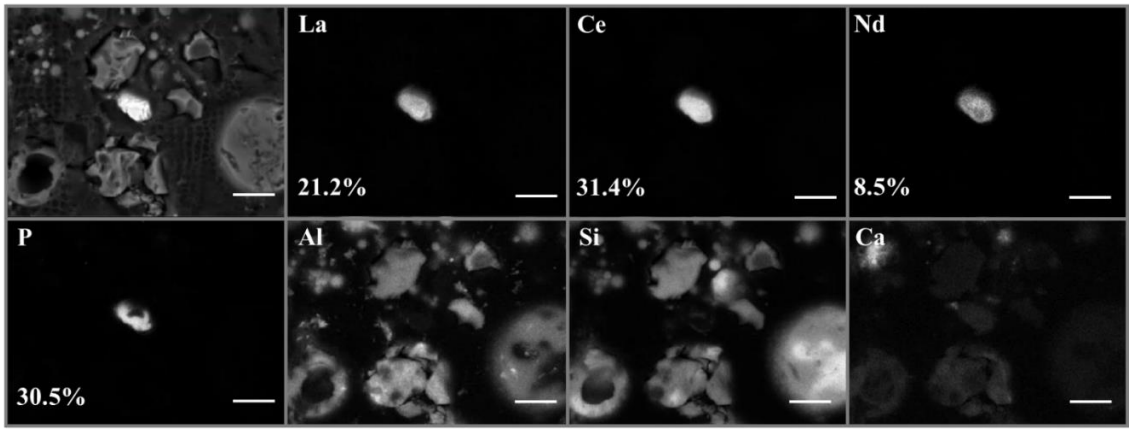

Figure 21: EPMA images of monazite in fly ash 345 obtained with backscattered electrons. Concentration of selected elements as determined by WDS is shown as weight percent (oxide). Scale bar is 10 µm.

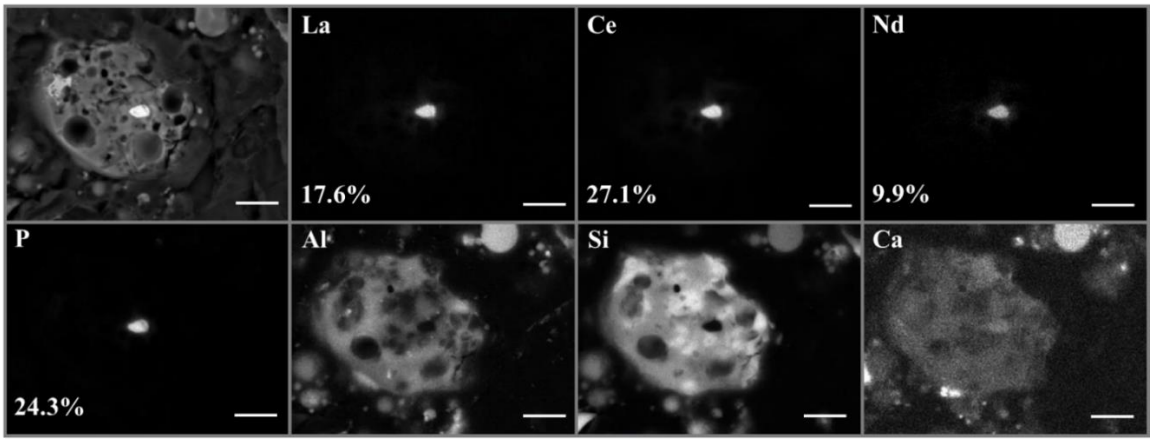

Figure 22: EPMA images of monazite encapsulated in Al/Si/Ca-rich glass obtained with backscattered electrons in fly ash sample 345. Concentration of selected elements as determined by WDS are shown as weight percent (oxide). Scale bar is 10 µm.

3.2.4 Sample 357: Bottom/Fly Ash

Sample 357 was composed of light brown and black particles and contained small black char fragments. Grain size distribution is heterogeneous and ranges from mm-sized angular rock fragments and agglomerated particles to micron sized spheres (e.g., aluminosilicate spheres). (Fig. 23; Appendix, Fig. A-2 and A-3).

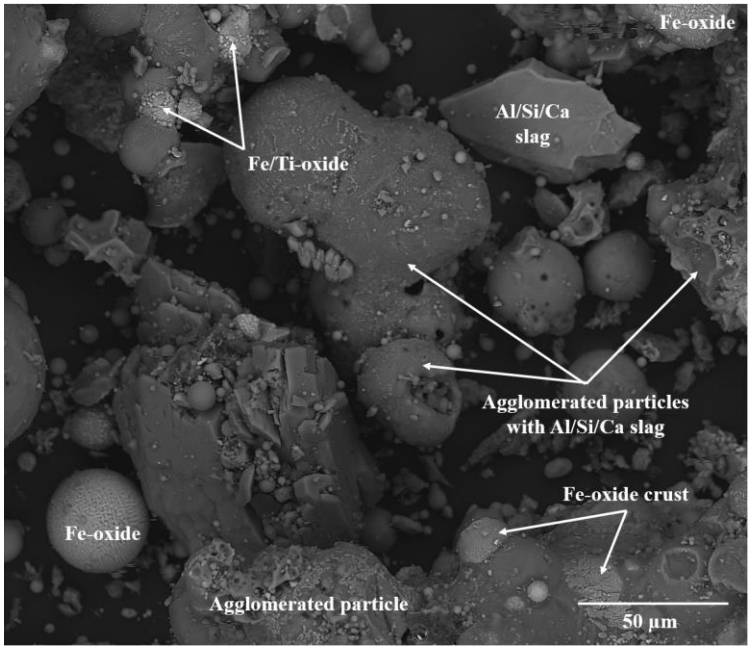

Figure 23: BSE image of grain mounted ash particles from sample 357.

The crystalline phases identified in the sample by XRD were mullite, quartz, magnetite and hematite (Table 3 and Appendix, Fig. A-1). The XRD pattern baseline was raised from 13^o to 40^o (2θ) indicating the presence of amorphous glass. The predominant particle types in the sample are a combination of aluminosilicate spheres (moderate), agglomerated particles and Al/Si/Ca slag (moderate), and Fe/Ti spherical particles (minor) (see Appendix, Table A-1). The remainder of the sample contained minor or trace amounts of Fe/Al/Si spheres, crystalline particles, unburnt carbon, and other types of particles (Appendix, Table A-1). Also abundant are mineral phases including hematite as solid droplets or spheres (Fig. 24a) and surficial coating of (Fe, Ca)-carbonate on aluminosilicate particles and slag (Fig. 24b). In this sample, there were Fe-oxide mineral crusts and flocculation that may have been dendritic (Fig. 23, bottom right; Fig. 25) or granular (Fig. 24) in nature.

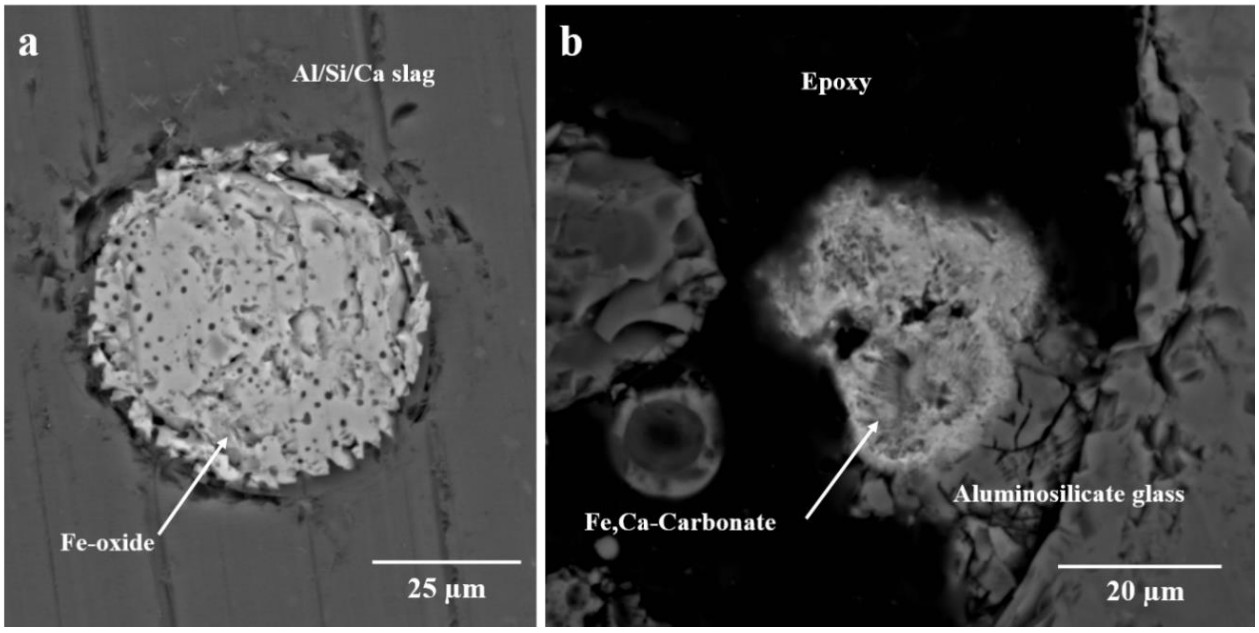

Figure 24: BSE images of (a) iron oxide solid particle in Al/Si/Ca slag and (b) iron-calcium carbonate fused to aluminosilicate glass.

A majority of the spherical particles were coated in thick (>5 micron) or fully encapsulated Al/Si/Ca slag (Fig. 23, 24 and 26). In some cases, calcium rich slag encapsulates smaller aluminosilicate glass particles or may become fused to surface of larger glass particles. In addition, calcium sulfate crystals, identified as gypsum by XRD, were present as mineral crystals and on the surface of larger agglomerated slag particles (see Fig. 25 and Appendix, Fig. A-1). Aluminosilicate particles and Fe/Ti oxide crusts were adsorbed to the surface of the gypsum crystals. In addition, iron sulfides (chemically similar to pyrite) were associated with unburnt carbon phases (Fig. 25).

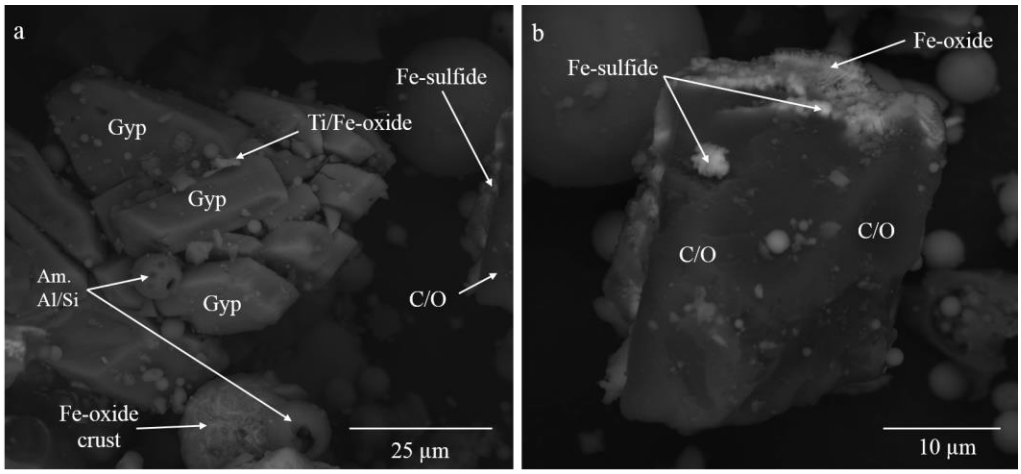

Figure 25: SEM-BSE images of (a) gypsum and (b) unburnt carbon particle (C/O) with mixed iron sulfide and iron oxide mineral crust.

Fifty percent of the agglomerated particles measured in the sample were in the size range of 40-60 microns in length (Appendix, Fig. A-3). Large agglomerated particles (>120 microns) make up 10% of the total particles measured. The maximum size measured during point counts was 288 microns. However, larger particles (up to 1 mm) are present in the sample (Fig. 26). Large agglomerated particles contained abundant aluminosilicate and iron oxide particles in a matrix of Al/Si/Ca slag material (Fig. 26).

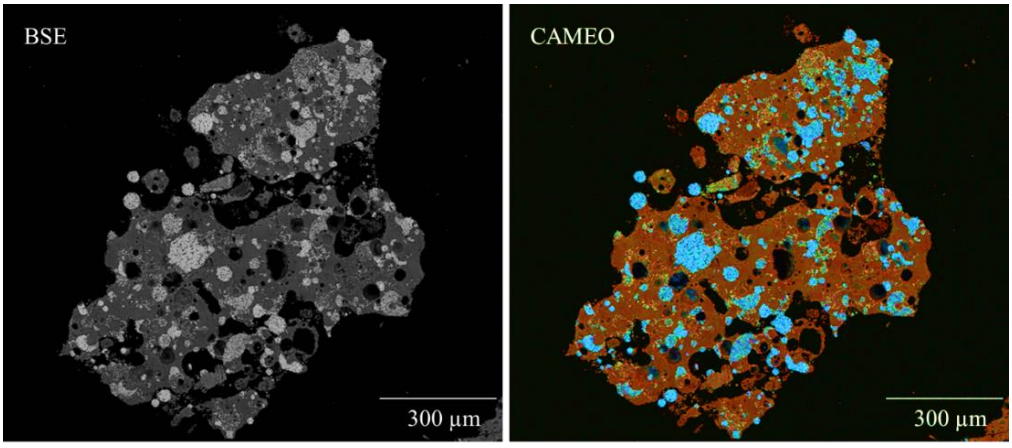

Figure 26: SEM-BSE image and a cameo image of an agglomerated particle composed of Al/Si/Ca slag (brown-red) containing Fe-oxide (blue) and Ca-rich (green) particles.

Characterization of bottom ash sample 357 revealed that no REE minerals phases were identified in SEM observations or XRD. In addition, pixel count and point measurements using SEM-EDS failed to detect any REE in the iron phases analyzed, minerals crusts or other surficial mineral particulates (e.g., Figs. 23-25) or in Al/Si/Ca-rich slag (Fig. 26).

4. DISCUSSION

The characterization of rock and pulverized coal combustion ash samples suggests much of the REE content in the samples may be too diffuse to measure via XRD and SEM. In the samples that contained identifiable REE phases (samples 443, 508, and 345), monazite (Ce, La, Nd-PO_4) and xenotime (Y,Yb-PO_4) were the predominant rare earth mineral phases present. These results are consistent with prior studies of domestic coal and coal utilization byproducts (Hower et al., 2015; Brownfield et al., 2004).

XRD analysis successfully identified the major and subordinate mineral constituents in the samples, but the REE minerals, if present, were well below the detection limit of conventional XRD. However, without extensive separation and concentration methods, the relatively trace quantities of REE, compared to other crystalline mineral phases in the ash, are not detectable by XRD. All ash samples contained a significant amount of amorphous material, as evidenced in the large background diffraction-scattering maxima or glass "hump" in the 20-40^o 2θ range indicating the presence of amorphous glass or iron oxide in samples 251, 345, 339, and 357 (Brownfield et al., 2004). Hematite and magnetite are the predominant crystalline iron mineral phases in ash, and are formed as a byproduct of oxygenated combustion and disintegration of coal mineral material containing pyrite. The disintegration of iron bearing phyllosilicates (e.g., chlorite/clinochlore) in the coal feed also provides an additional source of iron for the formation of hematite and other amorphous iron oxides that are present as coatings or crusts on ash particles.

After review of our complete data set, including SEM and EPMA results, we concluded that additional analysis is necessary to identify the clay minerals in the samples using oriented mounts for XRD. Additionally, a more suitable analysis is needed to quantify the percentage of amorphous material in each sample. Our methods employed whole peak fitting for quantification, which was suitable for a qualitative assessment of the samples. However, using the more robust standards-based Rietveld quantification to calculate the abundances of each crystalline clay phase can strengthen analysis. Note that many XRD databases lack the structural information for many minerals that is necessary to do Rietveld quantification, or data on the effect of varying types of amorphous materials on the X-ray patterns acquired.

The structure and thermal resistance of the source material (and potential corresponding REEs) could have implications for the viability of extraction processes. Rare earth minerals are embedded within the pore space of phyllosilicate minerals in rock samples and REE tends to be co-located with kaolinite grains. Monazite, when present in ash samples was observed as individual crystals in the ash matrix or as crystals that are fully encapsulated in glass (Figs. 20-23 and 27). Image processing, object classification and segmentation, allowed for the identification of REE mineral phases (e.g., monazite) in the fly ash matrix (Fig. 30). Electron probe microanalysis imaging and elemental mapping revealed the presence of REE (Ce, La, and Nd) in phosphate form and as the mineral monazite in fly ash sample 345. Monazite grains varying in size from 1-10 microns long were identified as an individual crystal in the ash matrix, encapsulated in aluminosilicate amorphous glass or inside hollow cenosphere (Figs. 20-22, 27, and 28).

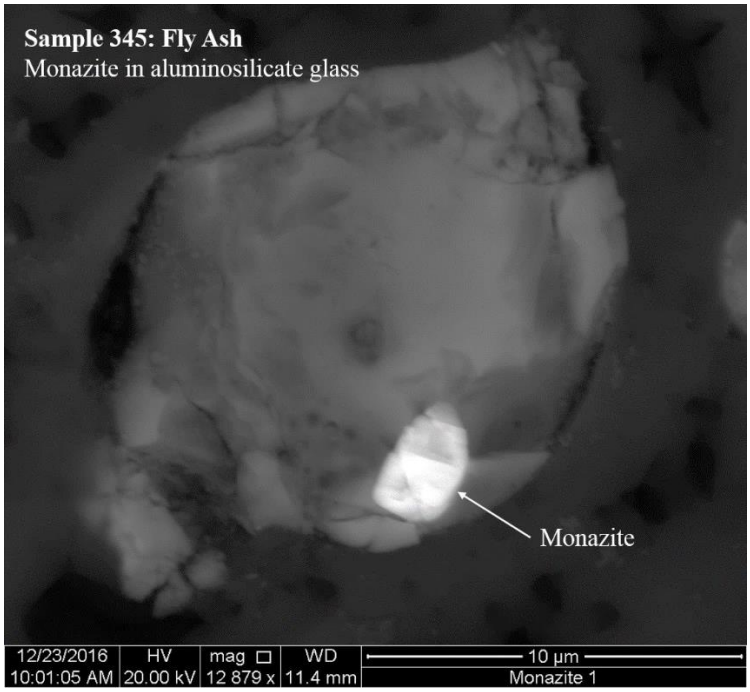

Figure 27: SEM-BSE image of a fly ash particle mounted in epoxy. The particle is composed of amorphous aluminosilicate glass and contains a monazite mineral grain.

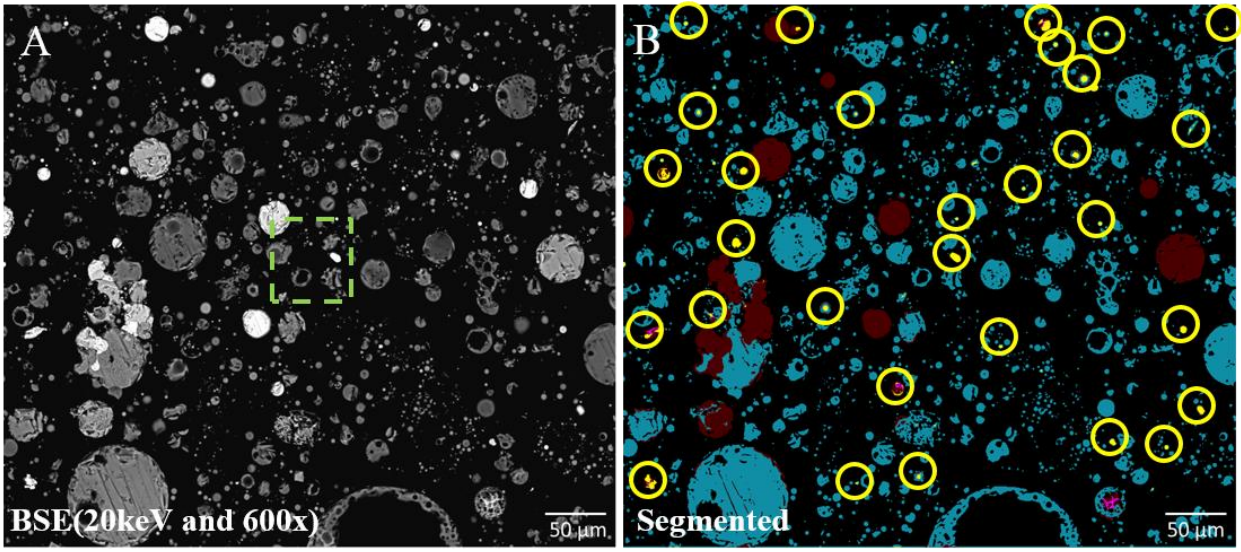

Figure 28: (Left) BSE image of fly ash particles from sample 345. The area within the green box was used for initial pixel/object classification. (Right) Mineral phases of fly ash (segmented image) are Al/Si-rich particles (blue), Fe-oxide (red), Monazite (yellow), and Al/Si/Ca oxide (pink).

Our observations support the hypothesis that some REE mineral grains, presumably phosphates such as monazite and xenotime, remain as crystalline minerals in ash and are unaltered and unaffected by the combustion process. REE-phosphate mineral phases are resistant to disintegration or decomposition, their structure and composition remain unaltered after combustion, and they remain in the ash matrix as unaltered mineral solids. The melting point of natural monazite ranges from 1916-2072ºC depending on which lanthanides are present (Sm<<La) (Hikichi and Nomura, 1987). Combustion of pulverized coal typically occurs at 1400-1600ºC (IEA Clean Coal Center 2010), therefore it is plausible that a large proportion of monazite and xenotime will remain in the ash as unaltered mineral solids. Minerals resistant to thermal decomposition during coal combustion could act as a nucleation site for the agglomeration of mixed element slag or glass during condensation and particle formation outside of the boiler (Meij, 1993). This process could lead to entombment of the REE mineral or other mineral phase with a melting point greater than ~1400ºC in the neo-formed glass (see Figs. 21 and 27; Appendix, Figs. A-5 and A-6) and prevent the extraction of REE without total dissolution of the slag and/or aluminosilicate glass.

Bulk elemental analysis of the samples by inductively coupled plasma mass spectrometry (ICP-MS), indicates that there are >300 ppm REE+Y. The lack of REE mineral grains observed by SEM or evidence for the formation of post-combustion secondary REE minerals in some fly and bottom ash samples supports our encapsulation hypothesis. In this case the REE minerals, presumably zircon, barite, and ilmentite, are also hidden within the glass matrix making it difficult to observe and quantify. An alternative hypothesis is that a large proportion of total REE are diffusely distributed throughout the ash matrix and difficult to detect using the current microanalytical techniques described.

The data presented in this report does not support the idea that combustion results in the complete melting of rare earth mineral phases, in this case monazite and xenotime, and redistribution of REE into secondary crystalline or amorphous phases associated with the surfaces of ash particles. The analyses presented indicates Al, Si, and Fe oxides in the ash do not contain REE. However, a more sensitive technique than SEM-EDS may be necessary to determine trace diffuse quantities (<1 wt.%) of REE. SEM-EDS analysis has identified Ce, La, and heavy REE (e.g., Y and Yb) in low concentrations (<2 wt. percent) associated with Ca oxide in fly ash samples 251 and 345. Since REE have a higher exchange rate with Ca, it is plausible that Ca oxides formed during the combustion process could incorporate REE. Similarly, trace amounts (~1% wt.) of REE (La) and Hf are present in pyrite from reject and roof rock. SEM-EDS was capable of detecting and quantifying the weight/atomic percent in phosphates in rock samples and ash. Our detection of monazite by SEM-EDS was confirmed with EPMA equipped with WDS. In general, quantifiable X-ray emissions from REE in surface coatings and crusts were not detectable. This may be due to the lack of REE in portions of the sample analyzed or difficulty in detecting X-rays from elements that may be below 1% by weight. It is also likely that the interaction volume of the X-rays makes it hard to capture the composition of the crust, which may only be a few microns thick. The detector would not pick up the limited counts.

One issue to note is the limitation in developing a full paragenetic sequence between the coal source and the ash formed for the materials in this study. Previous work (Hower et al., 1980) on the distribution of elements in coal combustion has identified a general paragenesis for the formation of and chemical composition of ash particles formed during combustion. Following the work of Hower et al. (1980), we can describe the following key mineral reactions and

transformations that likely control the chemical composition of the ash material and provide insight into the occurrence of REE in coal utilization byproducts.

1. Quartz- Crystalline quartz (measured by XRD)
2. Mullite- formed from thermal breakdown of aluminosilicate minerals in the coal feed
3. Aluminosilicate glass- Al and Si from the combustion of inorganic minerals in the coal, such as feldspars and clays results in the formation of amorphous glass material
4. Slag- Combination of Al, Si, K, Fe, and Ca from the decomposition of feldspars and clay (K from illite, or K-silicates if present; Fe from the breakdown of pyritic minerals or siderite in the coal feed; and Ca is from calcite or Ca-rich aluminosilicate in the coal feed)
5. Monazite, zircon, ilmentite, barite—Carried over from coal feedstock into the ash as monomineralic grains

5. CONCLUSIONS

The results of this work provide crucial information on the presence of REE and types of inorganic minerals present (e.g., oxides, phosphates, sulfates, sulfides) in coal utilization byproducts. This characterization report provides an elemental and mineralogical assessment of the coal ash and context to the partitioning of particular elements of interest into minerals formed during combustion.

The overarching conclusions of the study are:

- Monazite (LREE-PO_4) and xenotime (HREE-PO_4) coexist as isolated crystals with muscovite, kaolinite, and other phyllosilicates within parent rock and glass/slag materials in the coal refuse samples
- The presence of crystalline monazite and xenotime is a significant discovery showing that combustion has a limited impact on these phosphates. REE-PO_4 crystals are <10 μm in size
- Pixel and object classification of SEM-acquired images allows for the identification and quantification of REE minerals in CUB with different matrices.
- No REE-PO_4 was observed in fly ash sample 339 and bottom ash sample 357. High REE in ICP-MS analysis indicates that a large proportion of the REE may be encapsulated in ash mineral phases or as REE diffusely adsorbed to the surfaces of minerals or phases.
- FIB-SEM analysis yielded quantitative data on the volume of monazite grain in coal refuse demonstrating the ability to analyze and quantify the volume of REE mineral grains in a complex matrix. A robust volumetric reconstruction and combination with elemental measurements for minerals of interest can be used to better constrain resource estimates in both natural and engineered materials.

The microscopy and microanalysis results presented in this report provide a more robust characterization of the types of REE minerals present and the association between REE mineral phases and other particles in the ash. These analyses pinpoint key mineralogical and geochemical relationships that aid in the interpretation of bulk analyses (e.g., bulk ICP-MS results) used for resource evaluation. The workflow established an efficient way to identify and quantify REE mineral grains. Our characterization efforts used image montaging to scan large areas of the mounted material. Automated SEM-BSE imaging at magnifications up to 5000x with full elemental data, allowed the ability to stitch multiple images together, and perform automatic analysis using stacks of images (see Fig. 28). These image analysis techniques permit multiple (up to 1024) SEM fields of view to be simultaneously analyzed for specific minerals or elements of interest and expand the total area of sample that can be analyzed. Thus allowing us to scan large areas (up to 1 cm^2) of material and quantify the occurrence of REE minerals in a variety of different matrices.

6. REFERENCES

American Coal Association 2014 Coal Combustion Product (CCP) Produciton and Use Survey Report; 2014.

Brownfield, M. E.; Cathcart, J. D.; Affolter, R. H.; Brownfield, I. K.; Rice, C. A.; O'Connor, J. T.; Zielinski, R. A.; Bullock, J. H., Jr.; Hower, J. C.; Meeker, G. P. *Characterization and modes of occurrence of elements in feed coal and coal combustion products from a power plant utilizing low-sulfur coal from the Powder River Basin, Wyoming*; U.S. Geological Survey Scientific Investigations Report 2004-5271; 2005; p 36. http://pubs.usgs.gov/sir/2004/5271/

Franus, W.; Wiatros-Motyka, M. M.; Wdowin, M. Coal fly ash as a resource for rare earth elements. *Environ Sci Pollut Res.* **2015,** *22*, 9464-9474

Helble, J. J.; Sarofim, A. F. Trace element behavior during coal combustion. *Fuel* **1993,** *38*, 257-264.

Hikichi, Y.; Nomura, T.; Melting temperatures of Monazite and Xenotime. *Journal of the American Ceramic Society* **1987,** *70*, 252-253.

Hower, J. C.; Groppo, J. G.; Joshi, P.; Dai, S.; Moecher, D. P.; Johnston, M. N. Location of Cerium in Coal-Combustion Fly Ashes: Implications for Recovery of Lanthanides. *Coal Combustion and Gasification Products* **2013,** *5*, 73-78.

Hower, J. C.; Ruppert, L. F.; Eble, C. F. Lanthanide, yittrium, and zirconium anomolies in the Fire Clay coal bed Eastern Kentucky. *Intl. Jour. Of Coal Geol* **1999,** *39*, 141-153.

IEA Clean Coal Center 2010, Pulverized Coal Combustion, http://www.iea-coal.org.

Ketris, M. P.; Yudovich, Ya. E. Estimations of Clarkes for Carbonaceous biolithes: World averages for trace element contents in black shales and coals. *International Journal of Coal Geology* **2009**. doi:10.1016/j.coal.2009.01.002

Kutchko, B.; Kim, A. Fly ash characterization by SEM-EDS. *Fuel* **2006,** *85*, 2537-2544.

Mardon, S. M.; Hower, J. C. Impact of coal properties on coal combustion by product quality: examples from a Kentucky power plant. *Coal Geology* **2004,** *59*, 153-169.

Meij, R. Trace element behavior in coal fired power plants. *Fuel Processing Technology* **1993,** *39*, 199-217.

Moreno, N.; Querol, X.; Andres, J. M.; Stanton, K.; Towler, M.; Nugteren, H. Physicochemical characteristics of European pulverized coal combustion fly ashes. *Fuel* **2005,** *84*, 1351-1363.

Mulrooney, D.; Rivers, T. Redistribution of the rare earth elements among coexisting minerals in metamafic rocks across the epidote-out isograd: an exampl from the St. Anthony Complex, Northern New Foundland, Canada. *The Canadian Mineralogist* **2005,** *43*, 263-294.

National Energy Technology Laboratory Energy Data Exchange (NETL-EDX), Rare Earth Elements from Coal and Coal By-Products, https://edx.netl.doe.gov/ree/

National Energy Technology, Rare Earth Elements Program, 2016 Project Portfolio. http://netl.doe.gov/research/coal/rare-earth-elements

Rozelle, P. L.; Khadilkar, A. B.; Pulati, N. et al. A study on removal of rare earth elements from U.S. Coal byproducts by ion exchange. *Metallurgical and Materials Transactions E* **2016,** *3*. doi:10.1007/s40553-015-0064-7

Rudnick, R. L.; Gao, S. Composition of the Continental Crust. Treatise on Geochemistry. **2003,** *3*, 1-64.

Schatzel, S. J.; Stewart, B. W. Rare earth element sources and modification in the Lower Kittanning Bed, Pennsylvania: implications for the origin of mineral matter and rare earth element exposure in underground mines. *International Journal of Coal Geology* **2003,** *54*, 223-251.

Taggert, R. K.; Hower, J. C.; Dwyer, G. S.; Hsu-Kim, H. Trends in rare Earth Element Content of U.S.-Based Coal Combustion Fly Ashes. *Env. Sci and Tech.* **2016**, *50*. doi:10.1021/acs.est.6b00085

U.S. DOE, Coal Utilization By-products, U.S. Department of Energy Topical Report 24, August 2006.

United States Energy Information Administration (EIA), Monthly Energy Review, 2016. http://www.eia.gov/totalenergy/data/monthly/#coal

Warwick, P.D.; Crowley, S. S.; Ruppert, L. F.; Pontolillo, J. Petrography and geochemistry of selected lignite beds in the Gibbons Creek mine (Manning Formation, Jackson Group, Paleocene) of East Central Texas. *Int. J. Coal Geol.* **1997,** *34*, 307-326.

APPENDIX

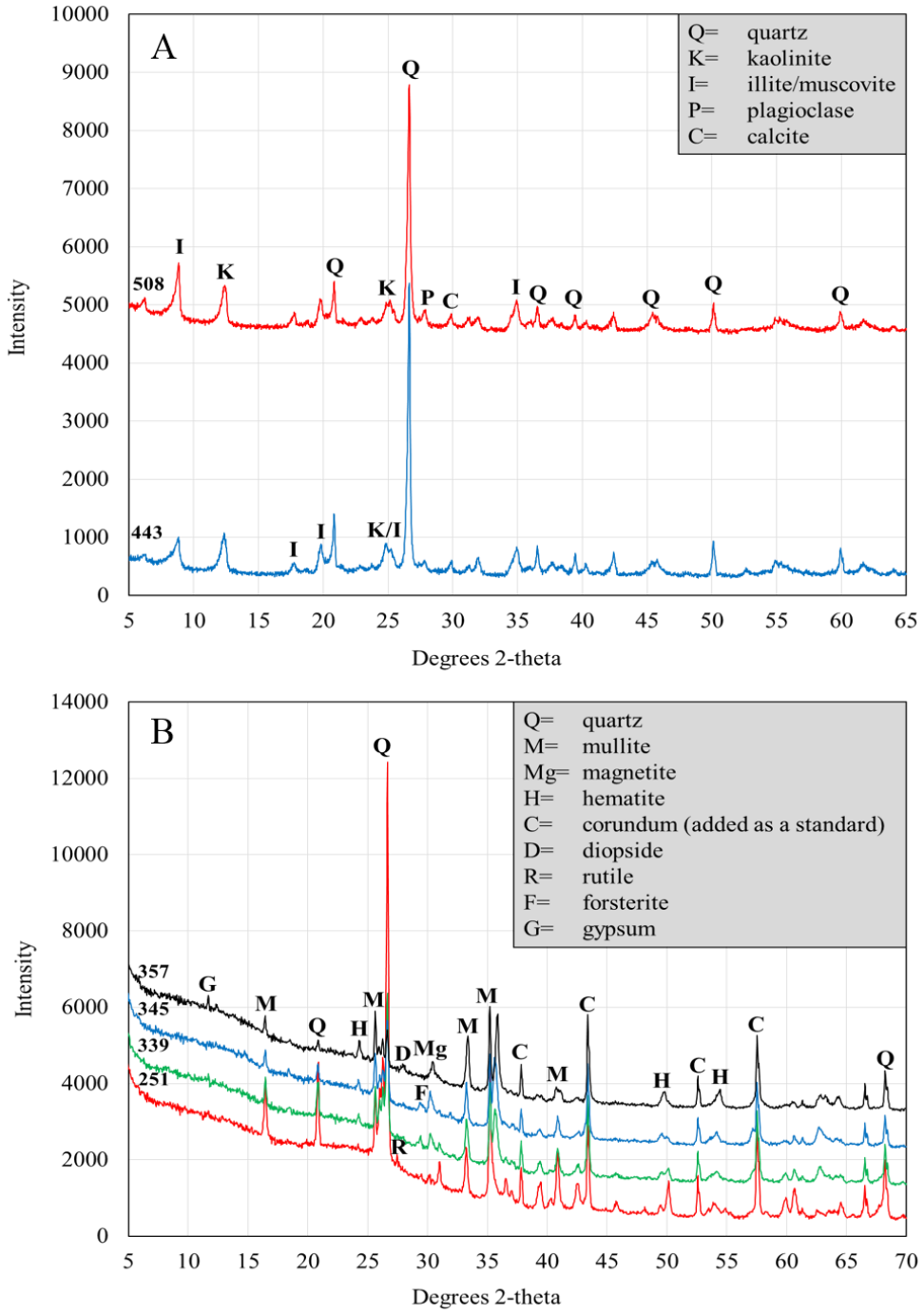

Figure A-1: A. Diffraction patterns for flint clay (443) and coal reject (508). B. Diffraction patterns for fly ash (251, 339, and 345) and bottom ash (357) samples spiked with ~10% NIST Al_2O_3 standard. The primary diffraction peaks for each crystalline component is identified.

Table A-1: Results for SEM point counts of ash samples. M-Med-Min-T-ND = major (>50%), medium (25-50%), minor (5-25%), trace (<5%), none detected.

	Al/Si-rich spheres	Fe/O-Al/Si-rich spheres	Fe/Ti/O-rich spheres	Ca-rich particles	Al/Si slag	Unburnt carbon	Crystalline minerals	Agglomerated particles
251	M	Min	T	T	T	T	ND	T
339	M	Min	Med	T	Min	Min	T	T
345	M	T	T	Min	T	T	T	Min
357	Med	T	Min	Min	Med	T	Min	Min

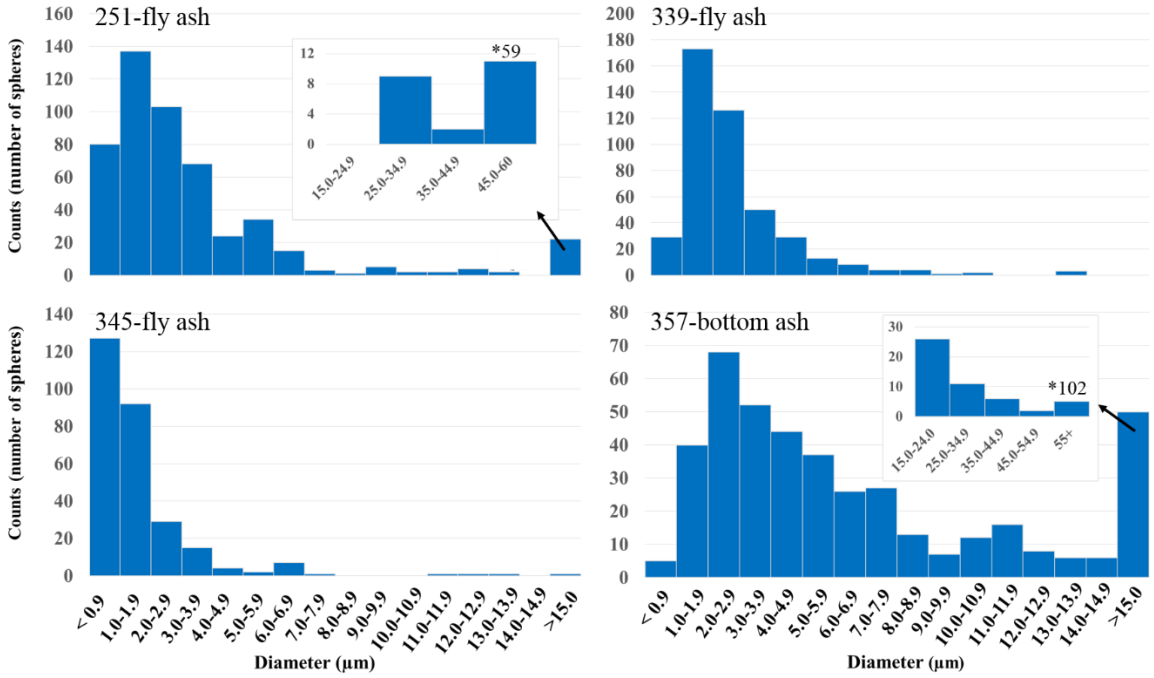

Figure A-2: Size distribution of spheres in fly and bottom ash samples as calculated SEM point counts. The maximum diameter measured for a single particle is denoted with an asterisk.

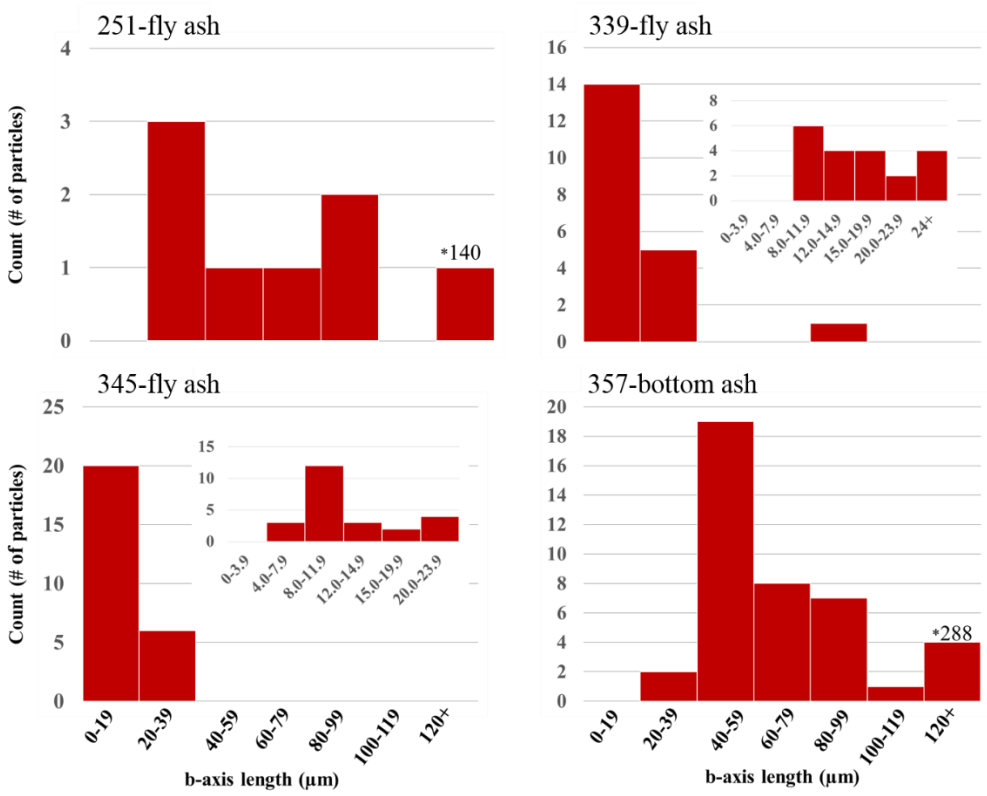

Figure A-3: Size distribution of agglomerated particles in fly and bottom ash samples as calculated from SEM point counts. The maximum b-axis length measured for a single particle is denoted with an asterisk.

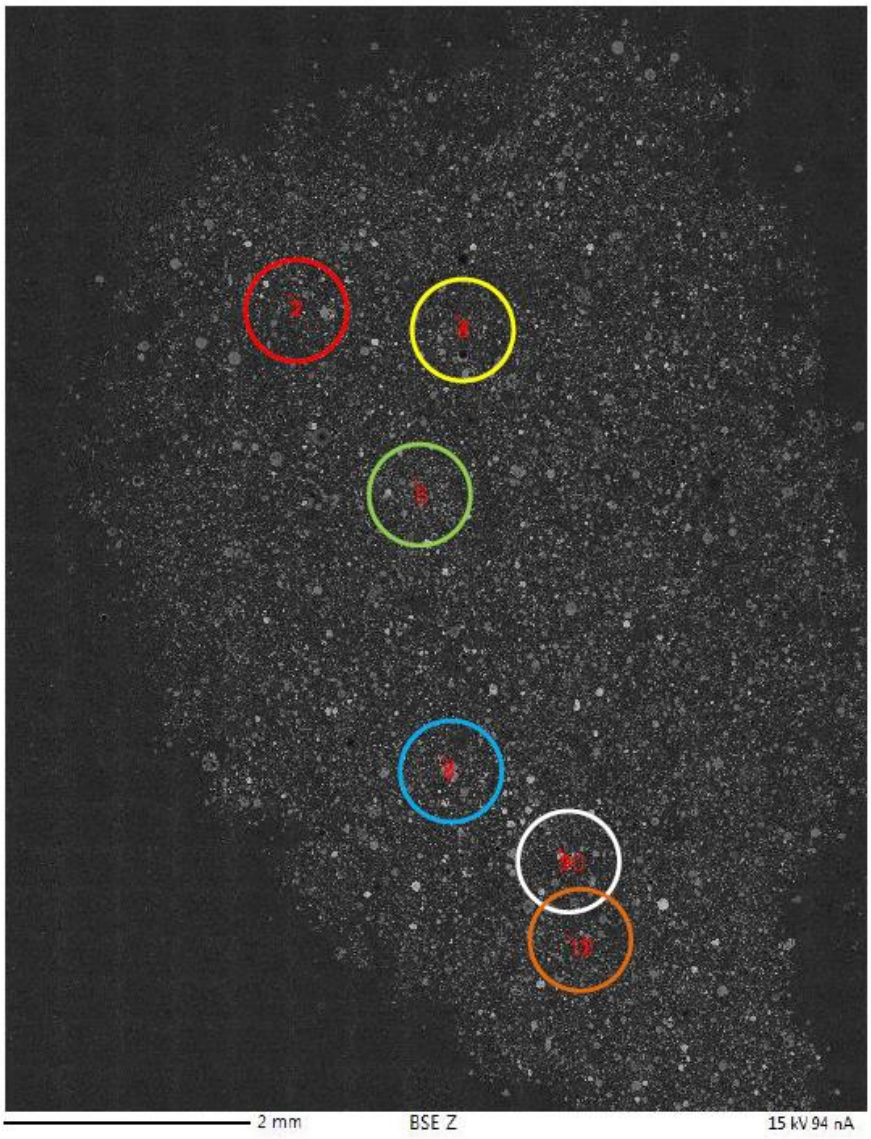

Figure A-4: Low magnification montaged EMPA-BSE image of fly ash particles from sample 345 mounted in epoxy. The colored circled areas are regions containing REE bearing minerals.

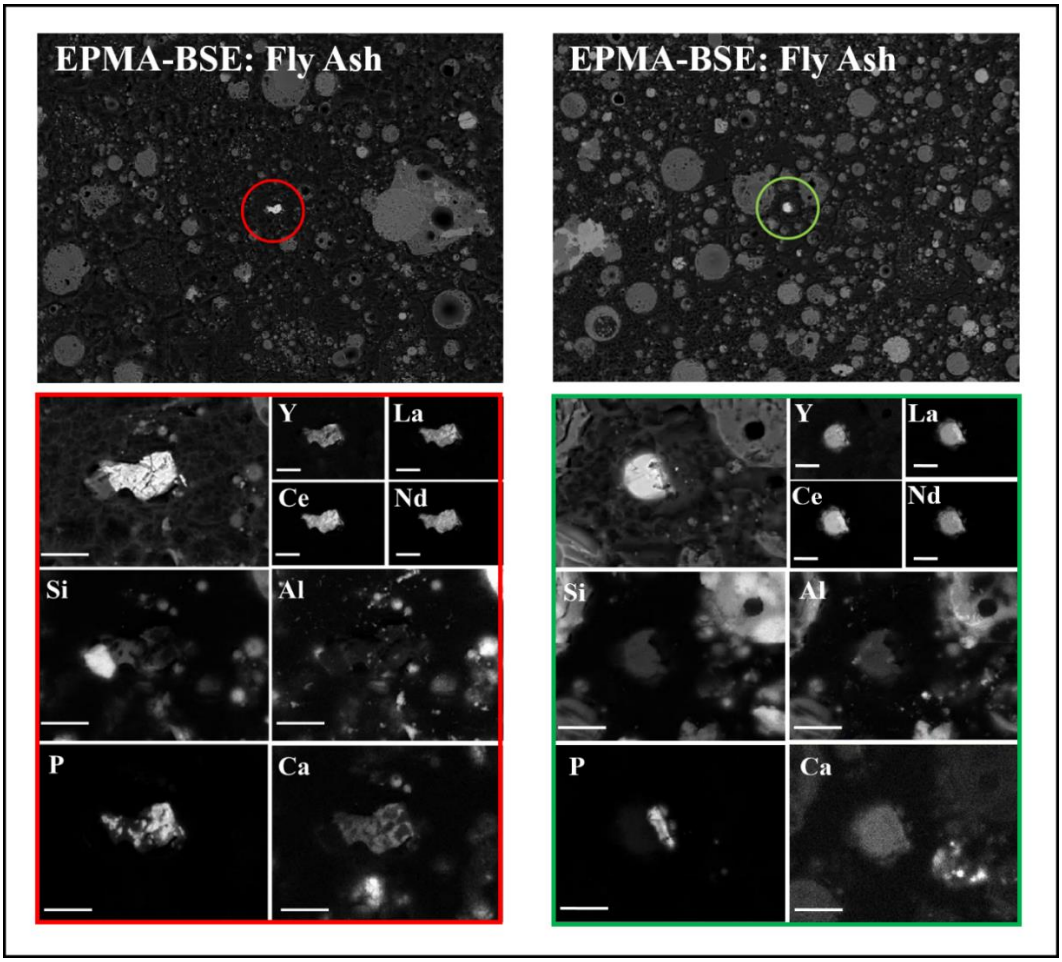

Figure A-5: EPMA-BSE images and EDS/WDS elemental maps for fly ash particles from sample 345. Scale bar is 10 µm.

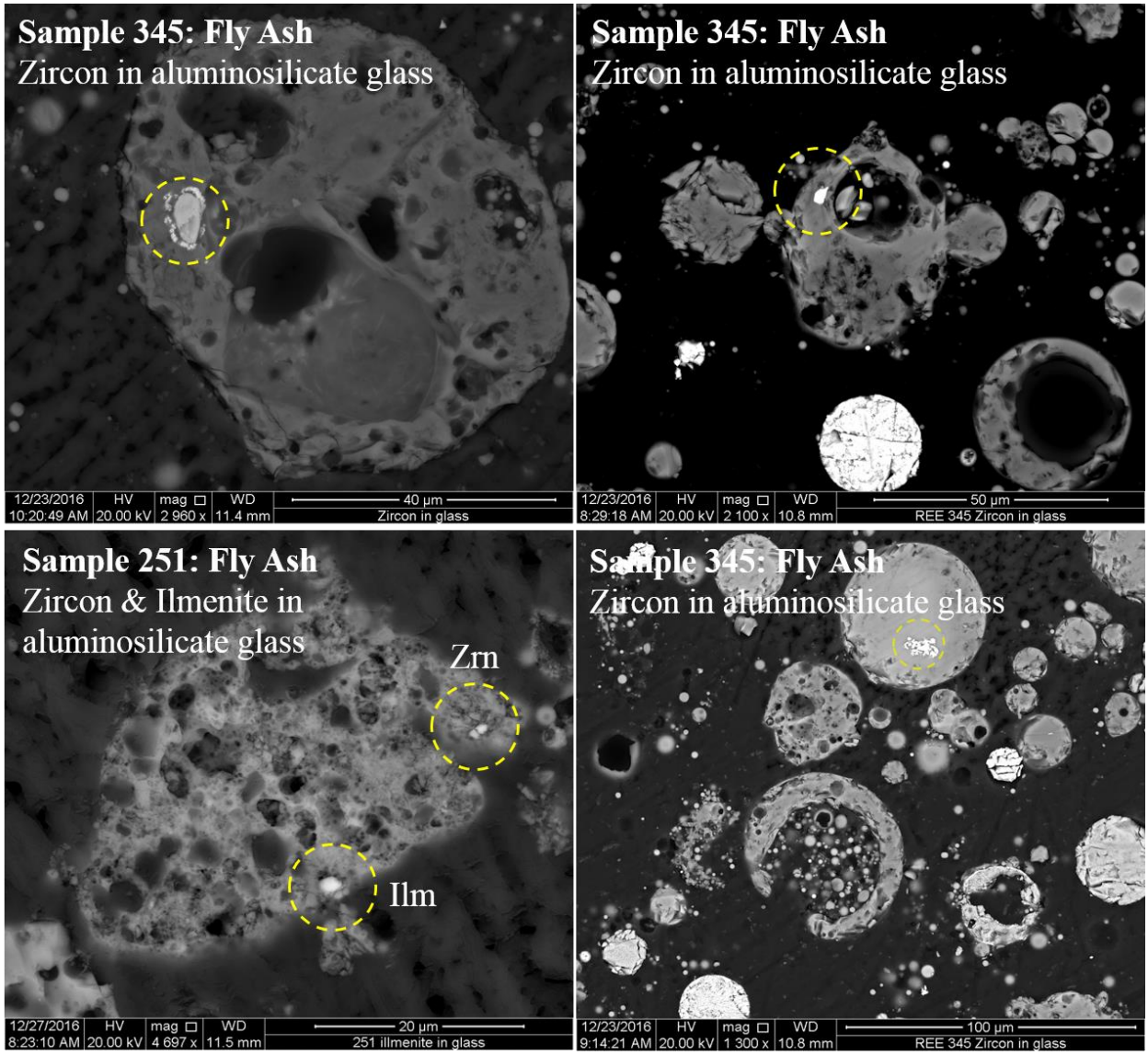

Figure A-6: SEM-BSE images of zircon (Zrn) and ilmenite (Ilm) encapsulated in aluminosilicate glass particles.

Mary Anne Alvin
Federal Technology Manager
Office of Research and Development
National Energy Technology Laboratory
U.S. Department of Energy

Regis Conrad
REE Program Manager Lead
Office of Fossil Energy
U.S. Department of Energy

Tom Tarka
Technical Portfolio Leader
National Energy Technology Laboratory

Charles Miller
Federal Project Manager
Strategic Center for Coal
National Energy Technology Laboratory
U.S. Department of Energy

David Alman
Executive Director
Research and Innovation Center
National Energy Technology Laboratory
U.S. Department of Energy

NETL Technical Report Series